PHYSICAL REVIEW D VOLUME 52, NUMBER 9 1 NOVEMBER 1995

# Calculation of the flux of atmospheric neutrinos

M. Honda and T. Kajita
*Institute for Cosmic Ray Research, University of Tokyo, Tanashi, Tokyo 188, Japan*

K. Kasahara
*Faculty of Engineering, Kanagawa University, Yokohama 221, Japan*

S. Midorikawa
*Faculty of Engineering, Aomori University, Aomori 030, Japan*
(Received 22 March 1995; revised manuscript received 14 June 1995)

Atmospheric neutrino fluxes are calculated over the wide energy range from 30 MeV to 3000 GeV for the study of neutrino physics using the data from underground neutrino detectors. In this calculation, a full Monte Carlo method is employed for low energy neutrinos (30 MeV–3 GeV), while a hybrid method is used for high energy neutrinos (1–3000 GeV). At low energies, the ratio $(\nu_e+\bar{\nu}_e)/(\nu_\mu+\bar{\nu}_\mu)$ agrees well with other calculations and is significantly different from observations. For the high energy neutrino fluxes, the zenith angle dependence of the atmospheric neutrino flux is studied in detail, so that neutrino oscillation parameters can be calculated for comparison with experimental results. The atmospheric muon flux at high altitude and at sea level is studied to calibrate the neutrino fluxes at low energies and high energies, respectively. The agreement of our calculation with observations is satisfactory. The uncertainty of atmospheric neutrino fluxes is also studied.

PACS number(s): 95.85.Ry, 13.85.Tp, 14.60.Pq

## I. INTRODUCTION

In this paper, we report the calculation of the atmospheric $\nu$ flux in the energy range from 30 MeV up to 3000 GeV, corresponding to the observation range of underground neutrino detectors. Detailed calculations of atmospheric $\nu$ fluxes are important, since the flux ratio $\nu_\mu/\nu_e$ observed by many experiments shows a significant deviation from the expected value [1–3] at low energies ($\langle E_\nu\rangle \sim 1$ GeV) and multi-GeV energies ($\langle E_\nu\rangle \sim 5$–7 GeV) [4]. Many authors have considered the possibility that this deviation is evidence for $\nu$ oscillations, with a large mixing angle and $\Delta m^2 \sim 10^{-2}$ eV$^2$ [1,5–8]. The zenith angle variation of the $(\mu/e)_{\rm data}/(\mu/e)_{\rm MC}$ ratio at multi-GeV energies is especially suggestive [4]. Above 10 GeV, upgoing $\mu$'s are used to determine $\nu_\mu$ fluxes. The variation of upgoing $\mu$ fluxes with the arrival direction can be used to study the oscillation parameters, since the distance to the place where $\nu$'s are produced is determined by the zenith angle of the arrival direction [9–11].

Atmospheric $\nu$ fluxes have been calculated by Volkova [12], Mitsui *et al.* [13], Butkevich *et al.* [14], and Lipari [15] mainly for high energies (from around 1 GeV to above 100 000 GeV). Gaisser *et al.* [16], Barr *et al.* [17], Bugaev and Naumov [18], Lee and Koh [19], and Honda *et al.* [20] calculated precisely the atmospheric $\nu$ flux for low energies ($\lesssim 3$ GeV). A calculation of low energy atmospheric $\nu$ flux using the $\mu$ flux observed at high altitudes has also been made [21].

In this paper, we use essentially the same models for particle interaction, atmospheric structure, and cosmic ray fluxes as Ref. [20]. The calculation method, however, is different for low energy (30 MeV to 3 GeV) and high energy (1–3000 GeV) atmospheric $\nu$'s. We employ a full Monte Carlo method at low energies, but use a hybrid method at high energies.

The difficulties in the calculation of atmospheric $\nu$ fluxes differ between high and low energies. In case of low energy $\nu$'s, the primary fluxes of cosmic ray components are relatively well known. However, the low energy cosmic ray fluxes ($\lesssim 30$ GeV) are modulated by solar activity, and are affected by the geomagnetic field through the rigidity (= momentum/charge) cutoff. For high energy $\nu$'s ($> 100$ GeV), the $\gtrsim 1000$ GeV cosmic ray flux is relevant. At these energies, solar activity and rigidity cutoff do not affect cosmic rays, but details of the cosmic ray flux are not as well measured. Details of the hadronic interactions of cosmic rays with air nuclei are also a source of the uncertainty in the calculated $\nu$ fluxes. At low energies, the proton-nucleus interaction at $\lesssim 30$ GeV is important. There have been many accelerator experiments studying hadronic interactions in this energy region; however, not many are suitable for our purpose. In the high energy proton-proton interactions, it is normally assumed that the spectrum of secondary particles satisfies the Feynman scaling hypothesis, which is confirmed by collider experiments up to a lab energy of 3000 TeV. Although there is a weak breaking of the hypothesis in the central region, it has no significant effect on atmospheric $\nu$ fluxes.

We employ a one-dimensional approximation in which all the secondary particles and the $\nu$'s keep the direction of their parent cosmic rays, throughout the energy range of concern. For high energy $\nu$'s, this is a good approxima-

 

tion because of the nature of hadronic interactions. We also expect that the directional average of $\nu$ fluxes may be calculated with good accuracy even at low energies. However, when we need information about the variation with direction of the low energy atmospheric $\nu$ flux, especially for near horizontal directions, a three-dimensional calculation is necessary. At low energies, secondary particles are produced with large scattering angles by hadronic interactions, and the curvature of low energy $\mu$'s due to the geomagnetic field becomes sizable. We note that a three-dimensional calculation of $\nu$ fluxes with the Monte Carlo method requires an enormous computation time, since we need to calculate the $\nu$ flux at every position on the Earth, and for all directions with good statistics.

Section II is devoted to the problems with low energy primary cosmic rays (Sec. II A), such as the effect of solar activity (Sec. II B) and the rigidity cutoff due to the geomagnetic field (Sec. II C). Also in Sec. II D, the primary cosmic ray fluxes are compiled for each chemical composition in the energy region of 100 GeV to 100 TeV, for use in the calculation of atmospheric $\nu$'s. The processes which take place during the propagation of cosmic rays in the atmosphere are explained in Sec. III. The hadronic interaction model we employ is explained in Sec. III A. The decay of mesons, such as $\pi$'s and $K$'s, which are created in cosmic ray interactions, is the main source of the atmospheric $\nu$'s. These decay processes are summarized in Sec. III B with a discussion of muon polarizations. In Sec. IV, we explain the calculation of atmospheric $\nu$ fluxes, and the results are summarized in Sec. IV B for 30 MeV to 3 GeV, and in Sec. IV C for 1–3000 GeV. In Sec. IV D, atmospheric $\mu$ fluxes are calculated by the same method as the $\nu$ fluxes, and are compared with the observed data. In Sec. V, the uncertainties in the calculation of atmospheric $\nu$ fluxes are discussed. In Sec. VI, the major results of this work are summarized.

## II. FLUX OF COSMIC RAYS

### A. Flux of cosmic rays below 100 GeV

Primary cosmic ray fluxes are relatively well known in the low energy region ($\lesssim$ 100 GeV), by which the low energy atmospheric $\nu$ fluxes ($\lesssim$ 3 GeV) are mainly created. However, the fluxes are affected by solar activity and the geomagnetic field. The effect of solar activity is known as the solar modulation of cosmic rays, and is commonly parametrized by the sun-spot number or the count rate of neutron monitors. The effect of the geomagnetic field is represented as the rigidity cutoff of cosmic rays. In the following, the treatment of these effects in this calculation is explained.

Webber and Lezniak have compiled the energy spectrum of primary cosmic rays for hydrogen, helium, and CNO nuclei in the energy range 10 MeV to 1000 GeV [22] for three levels of solar activity (Fig. 1). A similar compilation has been made by Seo *et al.* [31] for hydrogen and helium nuclei, which agrees well with that of Webber and Lezniak. Seo *et al.* estimated that uncertainties in the instrumental efficiency ($\sim$ 12%) and exposure factor (2–3 %) result in the overall uncertainty of the primary cosmic ray fluxes being $\sim$ 15% [31].

From the compilation of Webber and Lezniak, the chemical composition of cosmic rays is H(proton) $\sim$ 90.6%, He $\sim$ 9.0%, and CNO nuclei $\sim$ 0.4% above $\sim$ 100 MeV/nucleus, and H $\sim$ 95.2%, He $\sim$ 4.5%, and CNO nuclei $\sim$ 0.3% above $\sim$ 2 GeV/nucleus. The portion of other components (Ne, S, Fe, ...) is so small that they can be neglected in the calculation of low energy atmospheric $\nu$ fluxes. It is noted that atmospheric $\nu$'s are created through the hadronic interactions of cosmic rays and air nuclei, and therefore are dependent on the number of nucleons rather than the number of nuclei. The contribution of a heavier cosmic ray nucleus to the atmospheric $\nu$ flux is larger than that of a cosmic ray proton. Helium nuclei carry $\sim$ 15% of the total nucleons in the cosmic ray flux and the CNO group carries $\sim$ 3.6% above $\sim$ 2 GeV/nucleon. These effects are amplified by the effect of the geomagnetic field through the rigidity cutoff, since the rigidity for those nuclei is 2 times larger than protons with the same momentum/nucleon. The details are given below.

### B. Solar modulation

The flux of low energy cosmic rays is modulated by solar activity. The solar wind drives back the low energy cosmic rays which are entering into the solar sphere of influence, and the strength of the solar wind varies with solar activity. This effect is more evident in the lower energy cosmic rays: The flux difference at solar maximum and solar minimum is more than a factor of 2 for 1 GeV cosmic rays, and it decreases to $\sim$ 10% for 10 GeV cosmic rays (Fig. 1).

The primary flux for various levels of solar activity is parametrized by Nagashima *et al.* [32] as a function of the count rate of a neutron monitor $N$ by

$$f(E_k)dE_k = \gamma_i u^{-2.585} M(p,N) dE_k, \tag{2.1}$$

where $i$ stands for the kind of nucleus (=H, He, CNO,...), $p$ for rigidity in GV ($\equiv$GeV/$cZ$), $E_k$ for kinetic energy per nucleon in GeV, and $u$ for total energy per nucleon in GeV. The absolute flux value for each component is determined by $\gamma_i$, where $\gamma_{\rm H} = 10.85 \times 10^3$ m$^2$ sec$^{-1}$ sr$^{-1}$ GeV$^{-1}$, $\gamma_{\rm He} = 5.165 \times 10^2$ m$^2$ sec$^{-1}$ sr$^{-1}$ GeV$^{-1}$, and $\gamma_{\rm CNO} = 3.3 \times 10^{-2}$ m$^2$ sec$^{-1}$ sr$^{-1}$ GeV$^{-1}$ respectively. The function $M(p,N)$ is the modulation function defined by

$$M(p,N) = \exp\left[-\frac{1.15 + 14.9(1 - N/N_{\rm max})^{1.12}}{0.97 + (p/1\ {\rm GV})}\right], \tag{2.2}$$

and $N$ is the count rate of the neutron monitor at Mt. Washington with $N_{\rm max}$ = 2465 count/h. We take $N$ = 2445 for solar min, $N$ = 2300 for solar mid, and $N$ = 2115 for solar max. The results of the parametrization are shown in Fig. 1 by the solid, dashed, and dotted lines, which agree well with data except for low energy helium nuclei ($\lesssim$ 10 GeV/nucleon). However, this produces only a very small effect on the calculation of atmospheric $\nu$'s due to the proton dominance of the cosmic ray flux

and the relatively small contribution of cosmic rays of this energy.

### C. Rigidity cutoff of the geomagnetic field

The geomagnetic field determines the minimum energy with which a cosmic ray can arrive at the Earth. This effect is caused by the magnetic shield effect for low energy cosmic rays. For the cosmic ray nucleus, the minimum energy of cosmic rays arriving at the Earth is determined by the minimum rigidity (rigidity cutoff) rather than the minimum momentum. We note that the rigidity cutoff is a function of the entering position on the Earth and arrival direction (zenith angle $\theta$ and azimuth angle $\phi$). Since the mass/charge ratio of helium and CNO nuclei is twice that of protons, those nuclei carry lower energy nucleons into the atmosphere than protons.

The actual geomagnetic field is represented by a multipole expansion of the spherical harmonic function as

$$B_{\rm north} = \frac{1}{r}\frac{\partial V}{\partial \theta}, \quad B_{\rm east} = -\frac{1}{\sin\theta}\frac{\partial V}{\partial \phi}, \quad \text{and} \quad B_{\rm down} = \frac{\partial V}{\partial r}, \tag{2.3}$$

with the potential function

$$V = R\sum_{n=1}\sum_{m=0}^{n}\left(\frac{R}{r}\right)^{n+1}[g_n^m\cos(m\phi) + h_n^m\sin(m\phi)]P_n^m(\cos\theta). \tag{2.4}$$

Here $R$ is the radius of the Earth and $P_n^m(x)$ is the associated Legendre function. The expansion coefficient $(g_n^m, h_n^m)$ is compiled and reported by IAGA Division I working Group 1 [33]. As the geomagnetic field varies slowly with time, the coefficient is reported yearly with the time differential values.

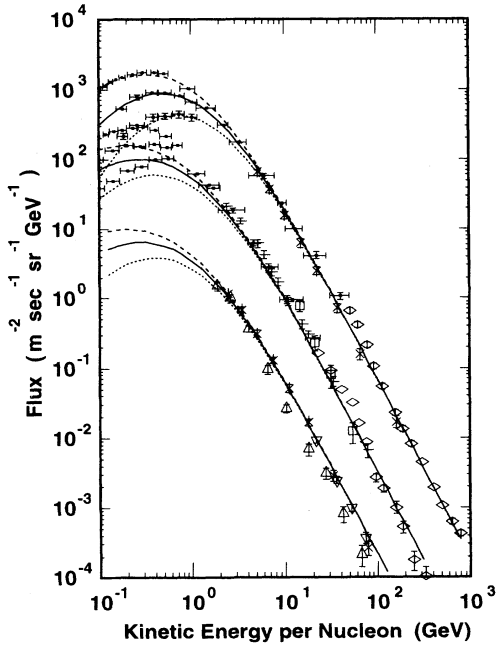


FIG. 1. Observed fluxes of cosmic ray protons, helium nuclei, and CNO's from the compilation of Webber and Lezniak [22]. (Dots represent data from Refs. [23] and [24], diamonds from Ref. [25], crosses from Ref. [26], minuses from Ref. [27], squares from Ref. [28], upward triangles from Ref. [29], and downward triangles from Ref. [30].) Solid lines are our parametrization for solar mid, dash lines for solar min, and dotted lines for solar max.

The value of the rigidity cutoff for the actual geomagnetic field can be obtained from a computer simulation of cosmic ray trajectories. In this simulation, an antiproton, which has the same mass as a proton but the opposite charge, is used as the test particle. We note that the change $e \leftrightarrow -e$ is equivalent to the change of $t \leftrightarrow -t$ in the equation of motion of a charged particle in a magnetic field:

$$\frac{\partial \mathbf{p}}{\partial t} = e\mathbf{v}\times\mathbf{B}, \tag{2.5}$$

where $\mathbf{p}$ is the momentum, $\mathbf{v}$ is the velocity, and $\mathbf{B}$ is the magnetic field. To determine the rigidity cutoff at different positions and for different directions, we launch antiprotons from the Earth, varying the position and direction. When a test particle with a given momentum reaches a distance of 10 times the Earth's radius, where the strength of the geomagnetic field decreases to the same level as the interstellar magnetic field ($\sim 3\times10^{-8}$ T), it is assumed that the test particle has escaped from the geomagnetic field. Assuming the momentum distribution of cosmic rays is isotropic in angular space, some cosmic rays which have the same rigidity can arrive at the Earth following the same trajectory but in the opposite direction. The rigidity cutoff is calculated as the minimum momentum with which the test particle escapes from the geomagnetic field. We note that for protons the rigidity and the momentum are the same quantity.

In a one-dimensional approximation, we need the rigidity for the arrival direction of $\nu$'s at $\nu$-detector sites. We found that the magnetic field calculated up to fifth order of the expansion gives almost the same result for rigidity cutoff as calculations with higher order expansions. The rigidity cutoff at Kamioka is shown as a contour map in Fig. 2. We note that the dipole approximation is good

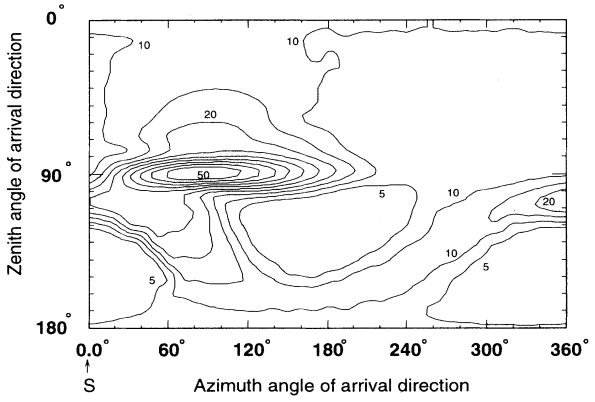


FIG. 2. The contour map of cutoff rigidity for the $\nu$ arrival directions at Kamioka. Azimuth angles of $0°, 90°, 180°$, and $270°$ show directions of south, east, north, and west, respectively.

near the magnetic equator. However, the multipole effect becomes important near the magnetic pole. For the calculation of atmospheric $\nu$ fluxes, we need the multipole expression for the geomagnetic field even when the detectors are not located near the pole, since $\nu$'s created near the pole arrive at the detector through the Earth.

### D. Cosmic ray fluxes above 100 GeV

Cosmic rays with energy greater than 100 GeV, which are responsible for $\gtrsim 10$ GeV atmospheric $\nu$ fluxes, are not affected by solar activity or by geomagnetic effects. However, there are few measurements of the cosmic ray chemical composition at these energies, especially above 1 TeV. Here, we compile the available data of cosmic ray fluxes for H, He, CNO, Ne-S, and Fe group nuclei up to 100 TeV/nucleon. Above 100 TeV/nucleon, the cosmic ray spectrum is measured by the air shower technique and almost no direct measurements of cosmic ray particles are available.

In Fig. 3, observed cosmic ray fluxes from

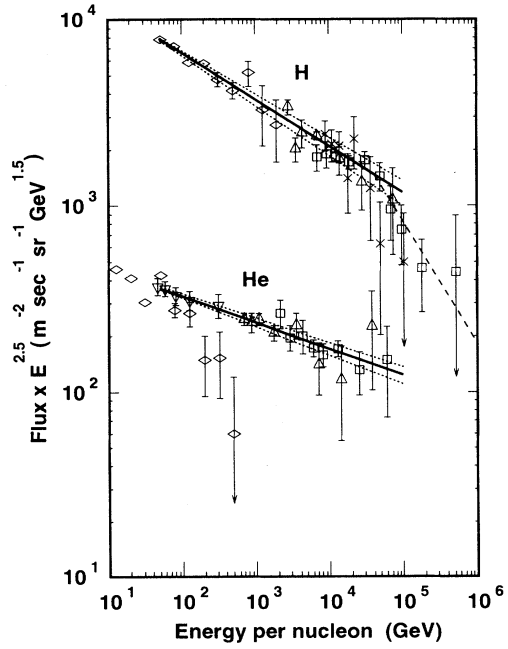


FIG. 3. The observed cosmic ray fluxes for H and He nuclei. The lines show our fits, as explained in the text. Diamonds are from Ref. [25], squares from Refs. [34] and [35], upward triangles from Ref. [36], downward triangles for He from Ref. [37], and crosses for H from Ref. [38]. The dashed line show the JACEE spectrum for H above 40 TeV [35].

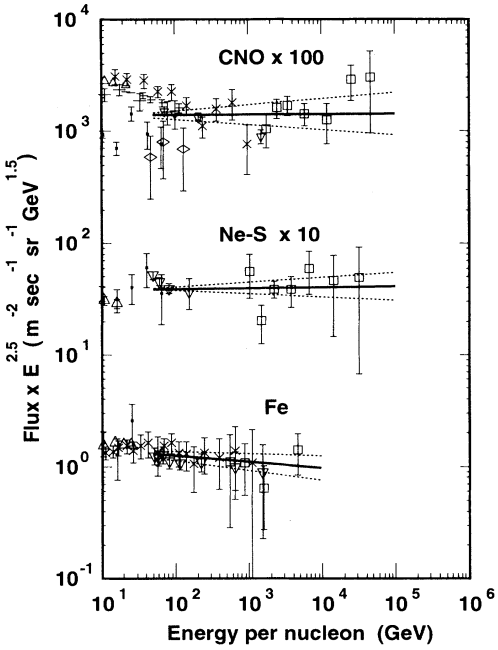


FIG. 4. Observed cosmic ray fluxes for CNO, Ne-S, and Fe nuclei. The lines show the fitted result as is explained in the text. Pluses are from Ref. [26], minuses from Ref. [30], squares from Ref. [35], crosses from Ref. [38], dots from Ref. [39], upward triangles from Ref. [40], downward triangles from Ref. [41], and diamonds from Ref. [42].

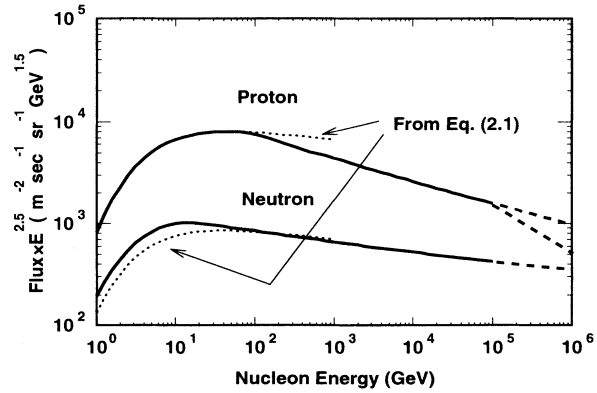


FIG. 5. The cosmic ray nucleon flux summed over all chemical components, and extrapolated (dashed line) up to 1000 TeV. The lower line for protons above 40 TeV assumes the steepening suggested by the JACEE group.

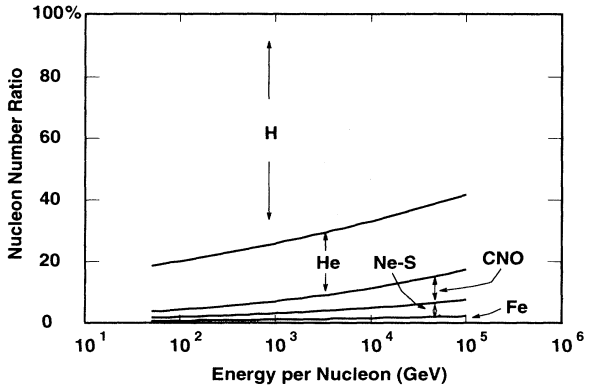


FIG. 6. Ratios of nucleons carried by H, He, CNO, Ne-S, and Fe group nuclei.

Refs. [25,34,36–38] are summarized for H and He. We fitted the observed flux for $\geq$ 100 GeV with a single power function:

$$\text{Flux}(E) = A(E/100\ \text{GeV})^{\gamma}\ , \tag{2.6}$$

and show the result in the same figure. We note that the data for He of Ryan *et al.* [25] are more than 2 times smaller than those of other groups and their error bars are larger than others. Therefore, we have not used their data in this analysis. The observed cosmic ray flux for CNO, Ne-S, and Fe group nuclei from Refs. [26,35,38,39,30,40,41] are shown in Fig. 4, also with our fitted spectra. The parameters $A, \gamma$ are summarized in Table I for H, He, CNO, Ne-S, and Fe group nuclei.

For the calculation of the atmospheric $\nu$ fluxes of energy region 1–3000 GeV, we employed the superposition approximation. This approximation treats a nucleus as a bundle of independent nucleons, and considers the event caused by the nucleus as the sum of independent events caused by these nucleons. Therefore, we need the flux of each nucleon rather than that of each chemical composition. In Fig. 5, we depicted the nucleon flux (proton and neutron) calculated from the single power function fit for H, He, CNO, Ne-S, and Fe group cosmic rays. For $<$ 100 GeV, we grouped the experimental points in Figs 1, 3, and 4 in several energy bins and calculated the average flux over different groups. Thus calculated proton flux below 100 GeV agrees well with the parametrization of Eq. 2.1 with $N$ = 2300 (solar mid), while the neutron flux is larger. This difference has already appeared in Fig. 1, but produces very small effects on the atmospheric $\nu$ flux as explained before. It is noted that the proton cosmic rays constitute $\sim$ 80% of all nucleons at 100 GeV/nucleon, and helium $\sim$ 15%. This percentage decreases with energy; however, $\sim$ 80% of nucleons are carried by proton and helium cosmic rays even at 100 TeV/nucleon (Fig. 6). The heavier nuclei are still a minor component of cosmic rays at this energy.

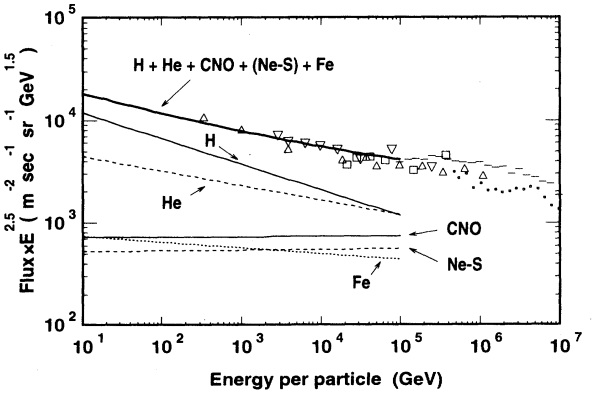


FIG. 7. The all-particle flux summed over fitted spectra for H, He, CNO, Ne-S, and Fe group nuclei compared with the observed data. Large squares from Ref. [35], downward triangles from Ref. [36], small squares are from Ref. [43], minuses from Ref. [44], and upward triangles from Ref. [45].

TABLE I. Fitted parameters for each chemical component of cosmic rays.

| Nucleus | $A(\text{m}^{-2}\,\text{sec}^{-1}\,\text{sr}^{-1}\,\text{GeV}^{-1})$ | $\gamma$ |
|---|---|---|
| H | $6.65 \pm 0.13 \times 10^{-2}$ | $-2.75 \pm 0.020$ |
| He | $3.28 \pm 0.05 \times 10^{-3}$ | $-2.64 \pm 0.014$ |
| CNO | $1.40 \pm 0.07 \times 10^{-4}$ | $-2.50 \pm 0.06$ |
| Ne-S | $3.91 \pm 0.03 \times 10^{-5}$ | $-2.49 \pm 0.04$ |
| Fe | $1.27 \pm 0.11 \times 10^{-5}$ | $-2.56 \pm 0.04$ |

Above 100 TeV, almost no observations of the cosmic ray chemical composition are available. However, the all-particle flux is measured well by the air-shower technique (e.g., see Ref. [43]). Converting the energy-per-nucleon spectra back to energy per particle, the H, He, CNO, Ne-S, and Fe group nuclei fluxes were summed and compared with the observed all-particle spectrum [35,36,43–45] in Fig. 7. It is seen that the extrapolation of the calculated all-particle flux agrees well with the experimental data even at energies above 100 TeV. We used the nucleon flux calculated here up to 1000 TeV (upper extrapolation for protons in Fig. 5). The JACEE group suggested that the spectrum of cosmic protons becomes steeper ($\gamma$ = 3.22) above 40 TeV [34] (see Fig. 3). The effect of this steepening has been studied for $\nu$ fluxes at 1000 GeV, but is very small. Errors in the cosmic ray nucleon spectra obtained here are estimated to be $\lesssim$ 10% at around 100 GeV and increase to $\sim$ 20% at 100 TeV.

## III. INTERACTION OF COSMIC RAYS IN AIR

### A. Hadronic interaction

As cosmic rays propagate in the atmosphere, they create $\pi$'s and $K$'s in interactions with air nuclei. These mesons create atmospheric $\nu$'s when they decay as

$$\begin{aligned} A_{\text{cr}} + A_{\text{air}} \rightarrow\ & \pi^{\pm}, K^{\pm}, K^0, \ldots \\ & \pi^+ \rightarrow \quad \mu^+ + \nu_\mu \\ & \qquad\quad \mu^+ \rightarrow \quad e^+ + \nu_e + \bar{\nu}_\mu \\ & \pi^- \rightarrow \quad \mu^- + \bar{\nu}_\mu \\ & \qquad\quad \mu^- \rightarrow \quad e^- + \bar{\nu}_e + \nu_\mu\ . \end{aligned} \tag{3.1}$$

The interactions of cosmic ray protons and nuclei with air nuclei are hadronic in character. We employed the NUCRIN [46] Monte Carlo code for hadronic interactions for lab energies $\leq$ 5 GeV, and the LUND code, FRITIOF version 1.6 [48] and JETSET version 6.3 [49], for 5 GeV $\leq E_{\rm lab} \leq$ 500 GeV. Above 500 GeV, the original code developed by Kasahara *et al.* (COSMOS) [50] was used. The $K/\pi$ ratio is taken as 7% at 10 GeV, 11% at 100 GeV, and 14% at 1000 GeV in lab energy. We compared the output of those codes with available experimental data. Although there have been many accelerator experiments of proton-nucleus and helium-nucleus interactions for $\lesssim$ 30 GeV, not many are applicable to our present purpose. For higher energies, the data of collider experiments are available for $p$-$p$ and $p$-$\bar{p}$ collisions. We estimate that the error of the atmospheric $\nu$ calculation resulting from these Monte Carlo codes is around 10%.

Results from the LUND code were compared with the $\pi$ production spectrum in a cone of $\leq 7.28°$ in $p$-Be collisions (24 GeV/$c$) [51] (Fig. 8). NUCRIN results were compared with the $\pi$ production spectrum at 2.5° in $p$-C collisions (5 GeV/$c$) [52] (Fig. 9). The agreement of the LUND code and experimental data is quite good ($\sim$ 10%) except for the very low momentum region ($\lesssim$ 5 GeV). Since the energy spectrum of cosmic rays is steep, the spectrum of $\pi$'s production by nucleons in the lower momentum region is relatively unimportant. The agreement of the NUCRIN code and experimental data seems not as good as that of the LUND code. The authors of the NUCRIN code estimated the disagreement of their output and experimental result as 10–20 % [47]. In low energy cosmic ray interactions, the detailed structure of the $\pi$ production spectrum may be smeared due to the flattening of the cosmic ray spectrum at low energies.

For high energies, it is difficult to get experimental results of nucleus-nucleus or proton-nucleus interactions. However, there are many results available from $p$-$\bar{p}(p)$ collider experiments. In Fig. 10, we present the experimentally determined pseudorapidity distribution for $\sqrt{s}$ = 53, 200, 546, and 900 GeV, and calculated results from the COSMOS and LUND codes for the same energies and $\sqrt{s}$ = 30.6 GeV, corresponding to a lab energy of 500 GeV. Above $\sqrt{s}$ = 53 GeV, the results of the COSMOS code agrees with the experimental results within $\lesssim$ 5%. Also the agreement of the COSMOS and LUND codes is good at $\sqrt{s}$ = 30.6 GeV. However, the pseudorapidity distributions calculated by the LUND code are lower than the experimental results and those of the COSMOS code near $\eta = 0$. Accordingly the multiplicity (the number of particles created by the interaction) in the LUND code is smaller than the experimental value above this energy. Therefore, above 500 GeV in lab energy we used the COSMOS code for hadronic interactions.

In the COSMOS code, nucleus-nucleus interactions are

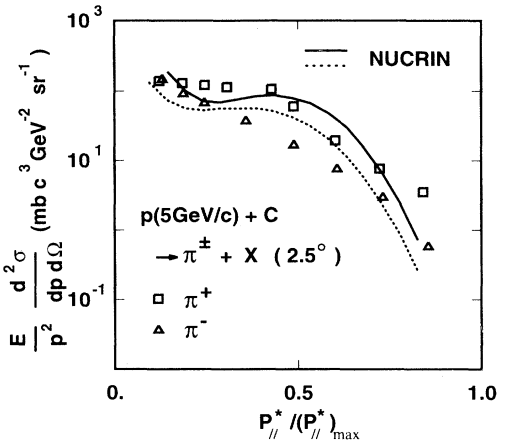


FIG. 9. Comparison of $\pi^{\pm}$-production spectrum in $p$-C collisions at $p$ = 5.1 GeV to the direction of 2.5° between experiment [51] and the NUCRIN Monte Carlo code. $P^*$ denotes the momentum in the total center of mass system.

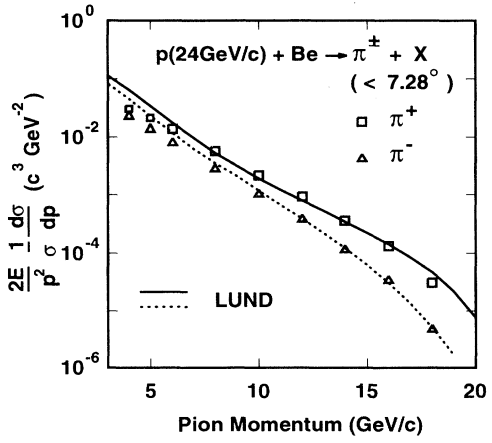


FIG. 8. Comparison of $\pi^{\pm}$-production spectrum in $p$-Be collisions at $p$ = 24 GeV/$c$ between experiment [50] and the LUND Monte Carlo code. The direction of the $\pi$'s are limited to $\leq 7.28°$ from the direction of projectile protons.

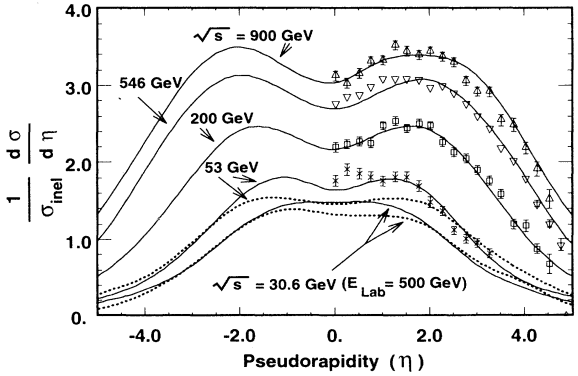


FIG. 10. Pseudorapidity distributions calculated by the COSMOS code (solid line). Upper triangles, downward triangles, and squares represent the data from UA-5, the CERN Super Proton Synchrotron ($Sp\bar{p}S$) [53], and crosses from UA-5, the CERN Intersecting Storage Rings (ISR) [54]. The dotted lines show the calculated results by LUND code.

treated as follows: First, the projectile (cosmic ray) nucleus fragments into smaller mass number nuclei and nucleons with given probabilities; second, each fragmented nucleon interacts with the target independently, and the sum of created particles in each interaction is considered as the product of the nucleus-nucleus interaction. We take the average number of nucleons which interact with the target (air) nucleus as

$$\langle N \rangle = A \frac{\sigma_p^{\rm inel}}{\sigma_A^{\rm inel}} , \tag{3.2}$$

where $A$ is the mass number of projectile nucleus and $\sigma_p^{\rm inel}$ ($\sigma_A^{\rm inel}$) is the inelastic cross section of the proton (nucleus) with the air nucleus. We used the full treatment of COSMOS for the calculation of $\nu$ fluxes in the 30 MeV to 3 GeV range, and the superposition model in the 1–3000 GeV range. The validity of the superposition model is discussed later (Sec. IV C).

A qualitative discussion of the hadronic interactions is useful in order to understand the $\nu_\mu$ and $\nu_e$ excess over their antiparticles. In hadronic interactions of low energy where one $\pi$ production is dominant, the projectile charge is most often carried by the leading particle. Thus, the most probable interaction for cosmic ray protons of this energy is

$$p + A_{\rm air} \rightarrow \ n + \pi^+ + X, \tag{3.3}$$

where $p$ stands for a proton and $n$ for a neutron. In the higher energy region where protons cause the multiple production, there also is a similar effect, that the $\pi^+$'s produced in this interaction statistically have a larger energy than $\pi^-$'s (see Fig. 8). Integrating with the steep spectrum of cosmic rays, there is an excess of $\pi^+$'s over $\pi^-$'s by $\sim$ 20 % for $\pi$ decay. Consequently, we expect $\sim$ 20% excess of $\nu_e$ over $\bar{\nu}_e$. We note that the neutron component of cosmic rays, which is carried by helium and other nuclei, creates a $\pi^-$'s excess over $\pi^+$'s from isospin symmetry. However, this gives a small effect on the $\pi$ spectrum and the atmospheric neutrino flux due to the proton dominance in the cosmic ray flux.

### B. Decay of mesons

Neutrinos are mainly produced in the following decays of $\mu$'s, $\pi$'s, and $K$'s [55]:

$$\begin{array}{lll}
\pi^\pm \rightarrow \mu^\pm \nu_\mu(\bar{\nu}_\mu) & (100\%), & \\
\mu^\pm \rightarrow e^\pm \nu_e(\bar{\nu}_e)\bar{\nu}_\mu(\nu_\mu) & (100\%), & \\
K^\pm \rightarrow \mu^\pm \nu_\mu(\bar{\nu}_\mu) & (63.5\%) & \\
\rightarrow \pi^\pm \pi^0 & (21.2\%) & \\
\rightarrow \pi^\pm \pi^+ \pi^- & (5.6\%) & \\
\rightarrow \pi^0 \mu^\pm \nu_\mu(\bar{\nu}_\mu) & (3.2\%) & (K_{3\mu\nu}) \\
\rightarrow \pi^0 e^\pm \nu_e(\bar{\nu}_e) & (4.8\%) & (K_{3e\nu}) \\
\rightarrow \pi^\pm \pi^0 \pi^0 & (1.73\%), & \\
K_s^0 \rightarrow \pi^+ \pi^- & (68.6\%), & \\
K_l^0 \rightarrow \pi^+ \pi^- \pi^0 & (12.37\%) & \\
\rightarrow \pi^\pm \mu^\mp \nu_\mu(\bar{\nu}_\mu) & (27\%) & (K_{3\mu\nu}) \\
\rightarrow \pi^\pm e^\mp \nu_e(\bar{\nu}_e) & (38.6\%) & (K_{3e\nu}).
\end{array} \tag{3.4}$$

The decay of charged $\pi$'s and subsequent $\mu$ decay ($\pi$-$\mu$ decay),

$$\begin{array}{l}
\pi^\pm \rightarrow \ \mu^\pm + \nu_\mu(\bar{\nu})_\mu \\
\qquad\quad \downarrow \\
\qquad\quad \mu^\pm \rightarrow e^\pm + \nu_e(\bar{\nu})_e + \bar{\nu}_\mu(\nu_\mu),
\end{array} \tag{3.5}$$

is dominant among these processes. Charmed particles, such as $D$ and $\bar{D}$, also create $\nu$'s; however, the contribution of charmed particles to atmospheric $\nu$'s becomes sizable only for $E_\nu \gtrsim 100$ TeV, which is far beyond the energy region of concern here.

When a $\pi^\pm$ decays at rest, the energy carried by $\nu_\mu(\bar{\nu}_\mu)$ is $(m_\pi^2 - m_\mu^2)/2m_\pi \sim 30$ MeV, and the $\mu^\pm$ carries the rest of the energy. If we ignore the spin of the $\mu$'s, each decay particle $e^\pm$, $\nu_e(\bar{\nu}_e)$, and $\bar{\nu}_\mu(\nu_\mu)$ carries 1/3 of $\mu^\pm$'s energy ($\sim$ 37 MeV) on average in the three-body decay. When $\pi$'s decay in flight, the $\pi$ energy is approximately divided into 1/4 to each decay product in the $\pi$-$\mu$ decay on average. Thus, we expect the flux ratio to be roughly $(\nu_e + \bar{\nu}_e)/(\nu_\mu + \bar{\nu}_\mu) = 1/2$ and $\bar{\nu}_\mu/\nu_\mu = 1$ irrespective of the $\pi$ spectrum. When the energy of the $\mu$'s becomes high ($\gtrsim$ 5 GeV), however, $\mu$'s tend not to decay in the air but to reach the Earth before decaying. In this case, $\mu$'s lose their energy in the Earth, and decay after they are almost stopped or are captured by nuclei in the Earth. This effect reduces the ratio $(\nu_e + \bar{\nu}_e)/(\nu_\mu + \bar{\nu}_\mu)$ above this energy. Also the ratio $\bar{\nu}_\mu/\nu_\mu$ decreases with energy in the same energy region, since cosmic ray protons create more $\pi^+$'s than $\pi^-$'s, and there is a corresponding excess of $\mu^+$'s over $\mu^-$'s. We note that $\mu$ polarization and $\mu$ energy loss in air are important for the precise calculation of atmospheric $\nu$'s. Each has $\gtrsim$ 5% effects on the $\nu$'s energy created by $\mu$'s. The energy loss of $\mu$'s in the air is taken into account by the Monte Carlo method. The treatment of $\mu$ polarization is explained in the following.

In the decay of charged $\pi$'s, the resulting $\mu^\pm$ is fully polarized against (toward) the direction of $\mu$ motion in the charged $\pi$ or $K$ rest frame. In the subsequent $\mu$ decay, $\nu_e(\bar{\nu}_e)$ is emitted to the forward direction of the $\mu$'s motion from the conservation of helicity. Thus the $\nu_e(\bar{\nu}_e)$ resulting from $\mu$ decay has a larger energy than $\bar{\nu}_\mu(\nu_\mu)$ in the $\pi$ rest frame. Since $\pi$'s decay in flight, the polarization is not full. In general, the direction distribution of $\nu_e$ is proportional to $(1 + \zeta \cos\theta)$ where $\zeta$ is the polarization ($\zeta = 1$ is full polarization) and $\theta$ is the angle between directions of $\nu_e$ motion and $\mu$ spin in the c.m. frame of the $\mu$'s. Practically, it is the polarization in the observer's frame that is important. Using the spin direction three-vector $\vec{\zeta}$, the polarization along the $\mu$ momentum direction is

$$\zeta = \vec{\zeta} \cdot \frac{\vec{p}}{|\vec{p}|} = \frac{E E^* - \gamma_\pi m_\mu^2}{\vec{p} \cdot \vec{p}^*} \tag{3.6}$$

in the observer's frame [56]. Here $E$ is the $\mu$ energy, $\vec{p}$ the $\mu$ momentum, and $\gamma_\pi$ is the Lorentz factor of the $\pi$ in observer's frame. $E^*$ and $\vec{p}^*$ denote the $\mu$ energy and the momentum in the $\pi$ rest frame, respectively.

The above discussion can also be applied to $\mu$'s created in the $K^\pm \rightarrow \mu^\pm \nu_\mu(\bar{\nu}_\mu)$ decay. For $\mu$'s resulting from the $K_{3l\nu}$ decay, the discussion in Ref. [57] is applied. The

small angle scattering of $\mu$'s in the atmosphere reduces the $\mu$ polarization. This depolarization effect is also evaluated by Hayakawa [56] as of the order of 21 MeV/$vp$, where $v$ and $p$ are velocity and momentum of $\mu$'s, respectively. Therefore, the depolarization effect may be negligible for $\mu$'s which produce $\nu$'s of energies $\gtrsim$ 100 MeV. If we ignore the effect of $\mu$ polarization, the calculated energy of $\nu_e$ decreases by $\sim$ 5% on average; therefore, the flux of $\nu_e$ is estimated to be smaller by $\sim$ 10% at 500 MeV and $\sim$ 15% at 3 GeV. This is an important effect for low energy $\nu$'s, which are observed in underground detectors [59].

## IV. FLUX OF ATMOSPHERIC NEUTRINOS

### A. $\nu$ fluxes and atmospheric density structure

We note first that the density structure of the atmosphere is important, because it is the reason for a large zenith angle dependence of $\nu$ fluxes. We take the U.S. standard [60] for the density structure of the atmosphere. The chemical composition of atmosphere is approximated by nitrogen 78%, oxygen 21%, and argon 1% in our calculation. For $\pi$'s and $K$'s propagating in the atmosphere, the decay and interaction with air nuclei are competitive processes. When the relation

$$c\tau\frac{E}{mc^2} \sim \frac{1}{\sigma n} \tag{4.1}$$

is satisfied, both processes work at nearly the same rate. Here, $\tau$ is the lifetime of the meson, $E$ is the energy, $\sigma$ the interaction cross section of the meson and air nuclei, and $n$ the number density of air nuclei. This condition (4.1) is rewritten for the energy of mesons with which decay and interaction take place almost equally as

$$E \sim \frac{mc^2}{c\tau\sigma n} = \left\{ \begin{array}{l} 12 \text{ (GeV for } \pi^{\pm}) \\ 22 \text{ (GeV for } K_L^0) \\ 90 \text{ (GeV for } K^{\pm}) \end{array} \right\} \times \frac{\rho_{[\text{sea level}]}}{\rho} , \tag{4.2}$$

where $\rho_{[\text{sea level}]} = 1.225\ \text{kg m}^{-3}$. Most mesons which have smaller energies than that given by this equation decay. Slant entering cosmic rays interact with atmospheric nuclei at a higher altitude than vertically entering cosmic rays on average. Therefore, the decay probability is larger for the mesons created by slant entering cosmic rays than for those of vertical cosmic rays. We expect a larger $\nu$ flux from near horizontal directions than from the vertical.

The first interaction of vertical cosmic rays takes place at an altitude of 15–20 km, where the density of air is $\sim$ 10 times less than that at the sea level, since the interaction mean free path (MFP) for cosmic ray protons is $\sim$ 100 g/cm$^2$ in column density. Mesons with energy $\lesssim$ 12 GeV, which create $\nu$'s of $\lesssim$ 3 GeV, decay before interacting with air nuclei. However, for mesons with energy $\gtrsim$ 100 GeV, the probability of interaction becomes sizable. Therefore, the variation of atmospheric $\nu$ fluxes with the zenith angle increases with the $\nu$ energy.

TABLE II. The low energy $\nu$ flux for Kamioka (solar mid, m$^{-2}$ sec$^{-1}$ sr$^{-1}$ GeV$^{-1}$).

| $E_\nu$ (GeV) | $\nu_\mu$ | $\bar{\nu}_\mu$ | $\nu_e$ | $\bar{\nu}_e$ |
|---|---|---|---|---|
| $3.162\times10^{-2}$ | 13845 | 14518 | 8616 | 8345 |
| $3.981\times10^{-2}$ | 14645 | 15097 | 8493 | 8232 |
| $5.012\times10^{-2}$ | 13805 | 13856 | 7238 | 6853 |
| $6.310\times10^{-2}$ | 11080 | 11154 | 5597 | 4995 |
| $7.943\times10^{-2}$ | 9113 | 9143 | 4539 | 3940 |
| $1.000\times10^{-1}$ | 7603 | 7568 | 3767 | 3272 |
| $1.259\times10^{-1}$ | 5913 | 5903 | 2916 | 2495 |
| $1.585\times10^{-1}$ | 4372 | 4372 | 2192 | 1851 |
| $1.995\times10^{-1}$ | 3124 | 3120 | 1597 | 1341 |
| $2.512\times10^{-1}$ | 2188 | 2180 | 1105 | 933 |
| $3.162\times10^{-1}$ | 1494 | 1486 | 752 | 636 |
| $3.981\times10^{-1}$ | 994 | 988 | 501 | 424 |
| $5.012\times10^{-1}$ | 647 | 641 | 322 | 274 |
| $6.310\times10^{-1}$ | 412 | 407 | 204 | 173 |
| $7.943\times10^{-1}$ | 256 | 252 | 127 | 107 |
| 1.000 | 155 | 152 | 75.7 | 63.9 |
| 1.259 | 90.9 | 87.9 | 44.3 | 37.4 |
| 1.585 | 52.3 | 49.7 | 25.2 | 21.0 |
| 1.995 | 29.6 | 27.9 | 13.7 | 11.1 |
| 2.512 | 16.4 | 15.4 | 7.10 | 5.96 |
| 3.162 | 8.92 | 8.32 | 3.65 | 3.19 |

### B. Low energy $\nu$ flux (30 MeV to 3 GeV)

At low energies, although the zenith angle dependence of $\nu$ fluxes caused by the atmospheric structure is not large, a significant directional variation is caused by the rigidity cutoff. In the one-dimensional approximation we adopted, we expect larger $\nu$ fluxes from the low rigidity cutoff direction and a smaller $\nu$ fluxes from the high rigidity cutoff direction. There should be a large directional-

TABLE III. The low energy $\nu$ flux for IMB (solar mid, m$^{-2}$ sec$^{-1}$ sr$^{-1}$ GeV$^{-1}$).

| $E_\nu$ (GeV) | $\nu_\mu$ | $\bar{\nu}_\mu$ | $\nu_e$ | $\bar{\nu}_e$ |
|---|---|---|---|---|
| $3.162\times10^{-2}$ | 26050 | 26869 | 15971 | 14170 |
| $3.981\times10^{-2}$ | 27302 | 27840 | 15725 | 13984 |
| $5.012\times10^{-2}$ | 25317 | 25453 | 13594 | 11816 |
| $6.310\times10^{-2}$ | 20437 | 20650 | 10778 | 8623 |
| $7.943\times10^{-2}$ | 16790 | 16744 | 8758 | 6765 |
| $1.000\times10^{-1}$ | 13807 | 13543 | 7129 | 5545 |
| $1.259\times10^{-1}$ | 10535 | 10430 | 5421 | 4155 |
| $1.585\times10^{-1}$ | 7509 | 7504 | 3955 | 3019 |
| $1.995\times10^{-1}$ | 5140 | 5153 | 2779 | 2135 |
| $2.512\times10^{-1}$ | 3494 | 3495 | 1868 | 1441 |
| $3.162\times10^{-1}$ | 2243 | 2260 | 1207 | 932 |
| $3.981\times10^{-1}$ | 1389 | 1404 | 758 | 590 |
| $5.012\times10^{-1}$ | 875 | 861 | 469 | 375 |
| $6.310\times10^{-1}$ | 528 | 524 | 280 | 223 |
| $7.943\times10^{-1}$ | 309 | 312 | 163 | 129 |
| 1.000 | 183 | 178 | 95.0 | 77.5 |
| 1.259 | 103 | 100 | 52.3 | 42.3 |
| 1.585 | 56.6 | 55.9 | 28.1 | 22.5 |
| 1.995 | 31.8 | 30.5 | 15.5 | 13.5 |
| 2.512 | 17.3 | 16.1 | 7.86 | 6.64 |
| 3.162 | 9.22 | 8.43 | 3.86 | 3.06 |

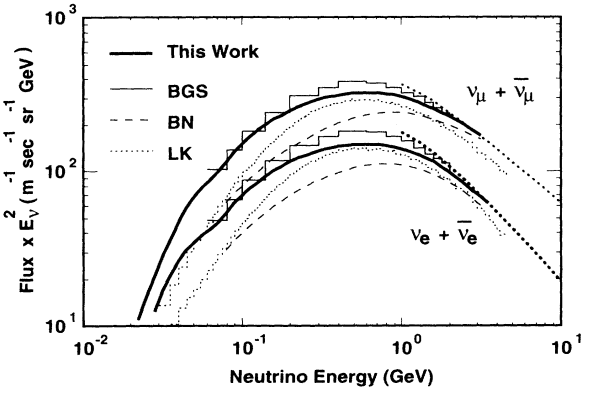


FIG. 11. The atmospheric $\nu$ fluxes multiplied by $E_\nu^2$ for the Kamioka site at solar mid (solid lines). BGS are from Ref. [16], BN from Ref. [17], and LK from Ref. [18]. The dotted line is the result from the calculation for high energy without the rigidity cutoff, and averaged over all directions. For details, see the next section (Sec. IV C).

dependent variation of $\nu$ fluxes for Kamioka (Fig. 2), especially a large deficit from east-horizontal direction. In the actual case, however, it may be difficult to observe those variations. The direction of a $\nu$ is different from that of the parent cosmic ray, because the mesons are produced with slightly different directions from that of incident particles, and again the $\nu$'s are created with slightly different directions from those of the mesons in their decay. We expect this effect to be rather small, but there is another smearing effect of direction in the $\nu$ detector. When a low energy $\nu$ ($\lesssim$ 3 GeV) creates a lepton by a quasielastic process, the lepton has a typical angle of 50°–60° from the $\nu$ direction [61]. Therefore, it may be difficult to observe the deficit of $\nu$ flux from east-horizontal direction in Kamioka. Thus the direction dependence of atmospheric $\nu$ flux is small for lower energy $\nu$'s, especially when they are observed in the detector. We present here the atmospheric $\nu$ flux, averaging over all directions.

For low energy $\nu$ fluxes, we employed a full Monte Carlo method. The calculation itself is rather straightforward. First, the nucleus and the primary energy of the cosmic ray are sampled with Eq. (2.1). Second, the arrival direction is sampled uniformly. When the rigidity is smaller than the rigidity cutoff, the cosmic ray is discarded. When the rigidity is larger than the rigidity cutoff, the cosmic ray is put to the propagation code of cosmic rays in the atmosphere, which controls the interaction of cosmic rays, the decay of secondary particles, and the energy losses in the atmosphere. The COSMOS code controls all these processes.

The results are summarized in Table II for Kamioka and in Table III for the IMB site, both for solar mid. Also in Fig. 11, $\nu_\mu + \bar{\nu}_\mu$ and $\nu_e + \bar{\nu}_e$ fluxes are depicted for Kamioka at solar mid, and compared with the other results. Since $\nu$ fluxes for solar mid are not available for other authors, we averaged solar max and solar min values. Flux differences between solar max and solar min are $\sim$ 8% at 100 MeV and $\sim$ 3% at 1 GeV for Kamioka, and $\sim$ 12% at 100 MeV and $\sim$ 4% at 1 GeV for IMB due to its lower cutoff rigidity. We note that these calculated results are smoothly connected to the atmospheric neutrino fluxes calculated by the hybrid method for high energies (1–3000 GeV) at around 3 GeV, where the effect of the rigidity cutoff is small.

In Fig. 12, we show the flux ratio by $\nu$ species along with those of other authors. We note that although the calculation method and some of the physical assumptions are different among these authors, the ratio $(\nu_e + \bar{\nu}_e)/(\nu_\mu + \bar{\nu}_\mu)$ is very similar. The relatively large difference in $\bar{\nu}_e/\nu_e$ among them may reflect the difference of calculation scheme and/or the physical assumptions.

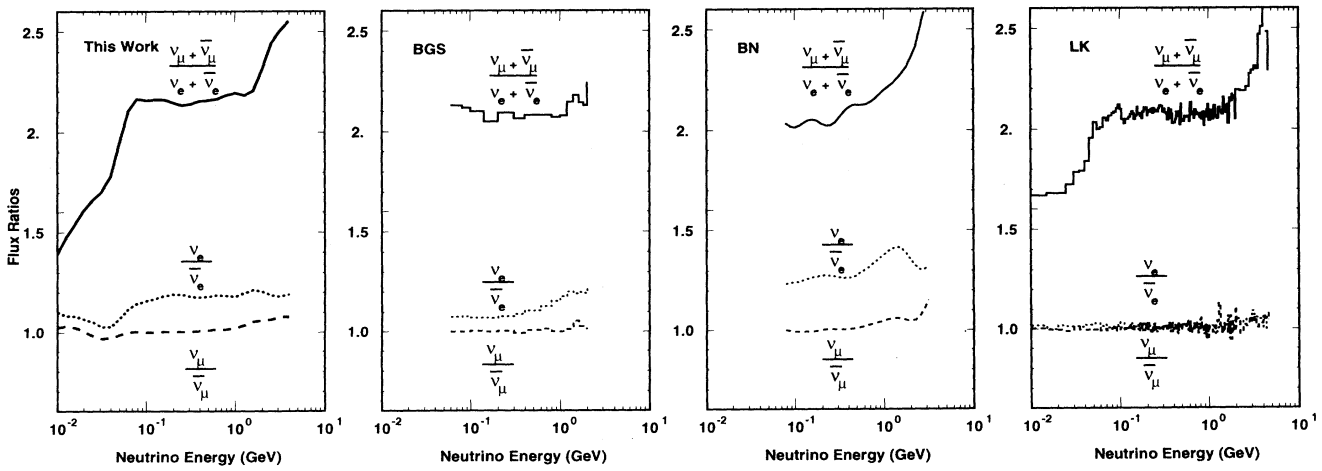


FIG. 12. The flux ratio of $\nu$ species calculated for Kamioka. BGS are from Ref. [16], BN from Ref. [17], and LK from Ref. [18], as before.

### C. High energy $\nu$ flux (1–3000 GeV)

For the calculation of atmospheric $\nu$'s at high energies (1–3000 GeV), we employed the superposition model and a hybrid method. We note that for helium nuclei, the complete treatment of COSMOS and the superposition model give essentially the same result. Let us measure the atmospheric depth by the column density from the top of the atmosphere. With Eq. (3.2), the average number of nucleons which interact with an air nucleus in a depth interval $[x, x+dx]$ is given by

$$\langle N\rangle e^{-\frac{x}{\lambda_A}}\frac{dx}{\lambda_A} = A\frac{\sigma_p}{\sigma_A}e^{-\frac{x}{\lambda_A}}\frac{dx}{\lambda_A} = A\frac{\lambda_A}{\lambda_p}e^{-\frac{x}{\lambda_A}}\frac{dx}{\lambda_A} \quad (4.3)$$

per nucleus. The nucleus MFP in the column density of air is denoted by $\lambda_A$, and the proton MFP denoted by $\lambda_p$. We note that $\sigma \propto 1/\lambda$. Since the fragmentation of helium nuclei into deuterons occurs with only a small probability, we can safely assume that helium nuclei always fragment into four nucleons $\{p,p,n,n\}$. The noninteracting nucleons at the first collision also interact with air nuclei in succeeding processes. The average number of nucleons which did not interact in the helium collision at the depth $x_1$ and that do interact in $[x, x+dx]$ is given by

$$(A-\langle N\rangle)\left[\int_0^x \frac{1}{\lambda_A}e^{-\frac{x_1}{\lambda_A}}\frac{1}{\lambda_p}e^{-\frac{x-x_1}{\lambda_p}}dx_1\right]dx$$

$$= A[e^{-\frac{x}{\lambda_p}} - e^{-\frac{x}{\lambda_A}}]\frac{dx}{\lambda_p} \quad (4.4)$$

for a nucleus. Adding (4.3) and (4.4), we get the average number of interacting nucleons in a depth interval $[x, x+dx]$ as

$$Ae^{-\frac{x}{\lambda_A}}\frac{dx}{\lambda_p} + A[e^{-\frac{x}{\lambda_p}} - e^{-\frac{x}{\lambda_A}}]\frac{dx}{\lambda_p} = Ae^{-\frac{x}{\lambda_p}}\frac{dx}{\lambda_p}, \quad (4.5)$$

which is exactly the same with the case of $A$-independent nucleons. We note that up to $E_{cr} = 100$ TeV, around 80% of all nucleons are carried by hydrogen and helium nuclei.

For heavier cosmic rays than helium, the probability of fragmentation into smaller nuclei (e.g., helium nucleus = $\alpha$ particle, etc.) is large at collisions. Therefore, the average number of nucleons which interact with the target (air) nucleus is smaller than that given by Eq. (3.2). Thus, the interaction height (depth) distribution of each nucleon is different from proton cosmic rays in general. This distribution is represented by the effective MFP of nucleons for heavier nuclei, and is calculated by the COSMOS code as $\sim 100$ g/cm$^2$ for CNO and $\sim 94$ g/cm$^2$ for Fe nuclei. The MFP is 87.4 g/cm$^2$ for protons, 36.6 g/cm$^2$ for CNO's, and 15.6 g/cm$^2$ for Fe nuclei at 1 TeV/nucleon. Thus the effective MFP for nucleons carried by those nuclei is more similar to the proton MFP than to those nuclei. These facts reasonably justify the superposition model, even for nuclei heavier than heliums.

In our hybrid method, we calculate the $\nu$-yield function for protons, $\eta_\nu^p(E, E_\nu, \theta)$, which denotes the number of $\nu$ in the energy region from $E_\nu$ to $E_\nu + dE_\nu$, created by a proton with energy of $E$ incident from the zenith angle $\theta$ with the Monte Carlo method. We executed the Monte Carlo simulation for proton cosmic rays with energies from 1 GeV to 1000 TeV in $\Delta \log_{10}(E_p) = 0.2$ steps, and for zenith angle bins of $\cos\theta = 0.0$–$0.1$, $0.1$–$0.2$, ...,

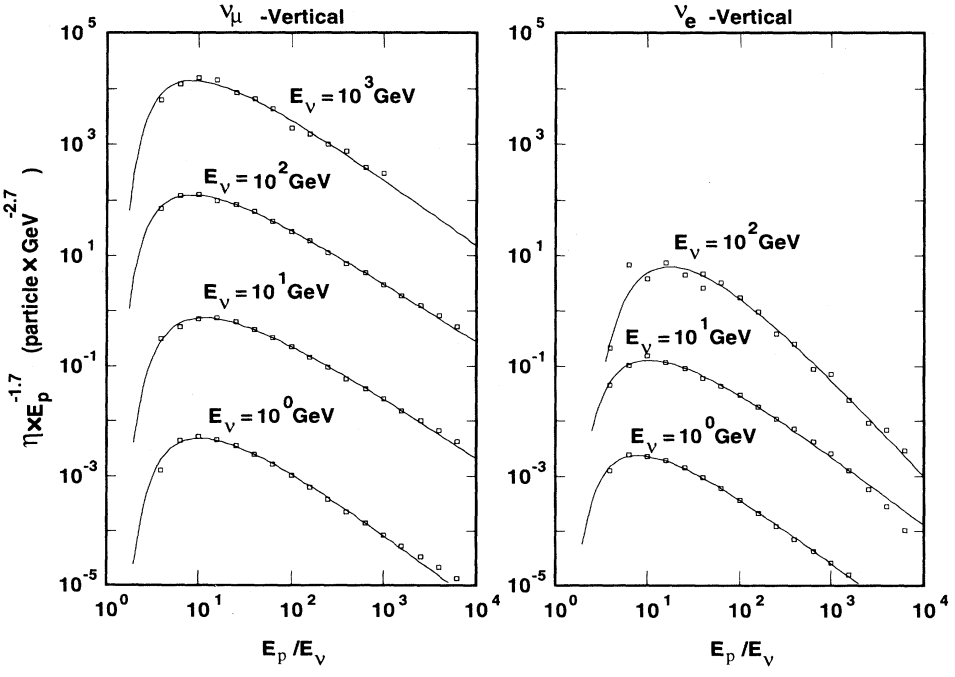


FIG. 13. $\nu$-yield function for protons with fixed $E_\nu$ multiplied by $E_p^{-1.7}$ for $\nu_\mu$ (left) and $\nu_e$ (right) for near vertical directions ($\cos\theta$= 0.9–1.0). Monte Carlo results are shown by squares, and fitted results by lines.

0.9–1.0. For each zenith angle bin, 300 000 protons were injected to the Monte Carlo code at 1 GeV, 100 000 protons at 10 GeV, ..., 1000 protons at 100 TeV, and 300 protons at 1000 TeV.

The proton $\nu$-yield function for $\nu_\mu$'s and $\nu_e$'s calculated by the Monte Carlo method is fitted by a function

$$F(E_p, E_\nu) = (E_p)^{-1.7} \times A \frac{[\log_{10}(E_p/E_\nu) - B]^2}{\log_{10}(E_p/E_\nu)} + C \ , \tag{4.6}$$

with parameters $\{A, B, C\}$. This fit agrees with the result of the Monte Carlo method very well in the region $3 \lesssim E_p/E_\nu \lesssim 10^3$, as seen in Fig. 13. The solid lines show our fit with Eq. (4.6). As the cosmic ray spectrum is approximately proportional to $E_{\rm cr}^{-2.7}$ in a wide energy range, the quantity shown in Fig. 13 roughly stands for the relative contribution to a fixed energy $\nu$'s from the cosmic ray in a logarithmic energy bin. The largest contribution to fixed energy atmospheric $\nu$'s comes from the cosmic ray with $E_{\rm cr} \sim 10E_\nu$ both for $\nu_\mu$'s and $\nu_e$'s. We note that the contribution from $E_p/E_\nu \lesssim 3$ and $E_p/E_\nu \gtrsim 10^3$ is very small($\lesssim 5\%$). The yield functions of $\nu_e$'s and $\bar{\nu}_e$'s decreases more rapidly than $\nu_\mu$'s and $\bar{\nu}_\mu$'s, and they change their shape for $E_\nu \gtrsim 100$ GeV.

For the neutron incident, we assumed

$$\eta_{\bar{\nu}}^p(E, E_\nu, \theta) = \eta_\nu^n(E, E_\nu, \theta)$$

and (4.7)

$$\eta_\nu^p(E, E_\nu, \theta) = \eta_{\bar{\nu}}^n(E, E_\nu, \theta) \ .$$

TABLE IV. $\nu_\mu$ flux $\times E_\nu^3$ ($\rm m^{-2}\,sec^{-1}\,sr^{-1}\,GeV^2$) calculated with the hybrid method. The value above $1 \times 10^4$ is the smooth extension with a power fit.

| $E_\nu$ (GeV)\ $\cos\theta$ | 0.0–0.1 | 0.1–0.2 | 0.2–0.3 | 0.3–0.4 | 0.4–0.5 | 0.5–0.6 | 0.6–0.7 | 0.7–0.8 | 0.8–0.9 | 0.9–1.0 |
|---|---|---|---|---|---|---|---|---|---|---|
| 1.000 | 213.5 | 208.0 | 202.1 | 195.8 | 189.1 | 182.2 | 176.1 | 170.7 | 165.9 | 161.9 |
| 1.259 | 245.1 | 237.3 | 229.2 | 221.0 | 212.6 | 204.3 | 196.9 | 190.5 | 185.0 | 180.4 |
| 1.585 | 275.5 | 264.5 | 253.8 | 243.4 | 233.4 | 223.8 | 215.4 | 208.2 | 202.1 | 197.0 |
| 1.995 | 302.8 | 288.0 | 274.2 | 261.5 | 249.8 | 239.0 | 229.7 | 221.9 | 215.4 | 210.2 |
| 2.512 | 327.1 | 308.3 | 291.5 | 276.4 | 262.8 | 250.8 | 240.7 | 232.3 | 225.7 | 220.5 |
| 3.162 | 349.6 | 327.1 | 307.3 | 289.9 | 274.6 | 261.2 | 250.2 | 241.4 | 234.6 | 229.7 |
| 3.981 | 370.6 | 344.4 | 321.7 | 302.1 | 285.1 | 270.5 | 258.7 | 249.5 | 242.7 | 238.0 |
| 5.012 | 390.6 | 360.4 | 334.7 | 312.9 | 294.5 | 279.2 | 266.9 | 257.4 | 250.4 | 245.8 |
| 6.310 | 409.4 | 374.7 | 346.0 | 322.3 | 302.9 | 287.2 | 274.7 | 265.0 | 257.9 | 253.1 |
| 7.943 | 427.2 | 387.7 | 355.7 | 330.2 | 309.9 | 294.2 | 281.6 | 271.8 | 264.3 | 259.2 |
| 10.00 | 444.5 | 399.4 | 363.9 | 336.4 | 315.4 | 299.8 | 287.2 | 277.1 | 269.2 | 263.5 |
| 12.59 | 460.8 | 409.7 | 370.5 | 340.9 | 319.2 | 303.6 | 291.0 | 280.6 | 272.3 | 265.8 |
| 15.85 | 475.6 | 418.2 | 375.2 | 343.5 | 321.0 | 305.6 | 293.0 | 282.3 | 273.3 | 266.0 |
| 19.95 | 488.7 | 424.9 | 378.0 | 344.3 | 321.0 | 305.7 | 293.0 | 281.9 | 272.3 | 264.1 |
| 25.12 | 500.0 | 429.6 | 378.9 | 343.1 | 319.1 | 303.9 | 291.1 | 279.6 | 269.3 | 260.2 |
| 31.62 | 509.6 | 433.1 | 379.0 | 341.4 | 316.7 | 301.5 | 288.5 | 276.6 | 265.7 | 255.7 |
| 39.81 | 517.6 | 436.4 | 379.5 | 340.4 | 315.0 | 299.7 | 286.5 | 274.2 | 262.7 | 252.1 |
| 50.12 | 523.9 | 439.4 | 380.5 | 340.2 | 314.2 | 298.4 | 284.9 | 272.3 | 260.4 | 249.3 |
| 63.10 | 528.4 | 442.2 | 382.0 | 340.8 | 314.1 | 297.8 | 283.9 | 270.8 | 258.7 | 247.4 |
| 79.43 | 531.2 | 444.6 | 383.9 | 342.1 | 314.7 | 297.8 | 283.3 | 270.0 | 257.7 | 246.3 |
| 100.0 | 532.1 | 446.7 | 386.3 | 344.2 | 316.2 | 298.4 | 283.2 | 269.6 | 257.2 | 246.1 |
| 125.9 | 531.7 | 448.0 | 388.1 | 345.9 | 317.2 | 298.4 | 282.6 | 268.6 | 256.3 | 245.3 |
| 158.5 | 530.4 | 448.0 | 388.5 | 346.1 | 316.6 | 296.9 | 280.4 | 266.0 | 253.6 | 242.9 |
| 199.5 | 528.2 | 446.8 | 387.4 | 344.6 | 314.5 | 293.7 | 276.6 | 261.9 | 249.3 | 238.7 |
| 251.2 | 525.2 | 444.3 | 384.9 | 341.6 | 310.8 | 289.0 | 271.2 | 256.2 | 243.5 | 233.0 |
| 316.2 | 521.3 | 440.6 | 380.9 | 337.1 | 305.5 | 282.9 | 264.5 | 249.0 | 236.2 | 225.8 |
| 398.1 | 516.4 | 435.1 | 374.9 | 330.6 | 298.4 | 275.2 | 256.3 | 240.7 | 227.8 | 217.4 |
| 501.2 | 510.3 | 427.2 | 366.1 | 321.4 | 289.0 | 265.7 | 246.8 | 231.3 | 218.6 | 208.3 |
| 631.0 | 503.0 | 417.3 | 355.0 | 309.9 | 277.6 | 254.6 | 236.1 | 220.9 | 208.5 | 198.5 |
| 794.3 | 494.6 | 405.4 | 341.7 | 296.4 | 264.5 | 242.3 | 224.5 | 209.8 | 197.8 | 188.2 |
| 1000.0 | 485.3 | 391.7 | 326.5 | 281.1 | 250.0 | 228.9 | 212.0 | 198.1 | 186.7 | 177.4 |
| 1259.0 | 474.4 | 375.7 | 308.8 | 263.5 | 233.4 | 213.7 | 198.1 | 185.1 | 174.3 | 165.3 |
| 1585.0 | 461.6 | 356.9 | 288.2 | 243.2 | 214.3 | 196.5 | 182.2 | 170.2 | 160.0 | 151.5 |
| 1995.0 | 447.1 | 335.8 | 265.4 | 220.9 | 193.7 | 177.8 | 165.0 | 154.1 | 144.6 | 136.5 |
| 2512.0 | 431.1 | 313.0 | 241.2 | 197.6 | 172.2 | 158.3 | 147.1 | 137.3 | 128.6 | 120.9 |
| 3162.0 | 406.0 | 296.5 | 228.2 | 185.2 | 158.4 | 142.0 | 128.8 | (117.5) | (107.8) | (99.44) |
| $10^4$ | (301.2) | (188.1) | (127.1) | (93.0) | (73.6) | ( 62.5) | (53.6) | (46.1) | (39.6) | (34.1) |
| $3.16 \times 10^4$ | (201.2) | (99.5) | (55.45) | (34.8) | (24.7) | (19.4) | (15.4) | (12.1) | (9.5) | (7.4) |

This assumption is justified for $\nu$'s produced through $\pi$'s, but not for those produced through $K$'s. The $K^-/K^+$ ratio is rather a universal quantity for $p$-$A$ and $A$-$A$ interactions ($\sim 0.8$) at high energies [58]. However, we note that the portion of proton nucleon is still $\sim 80\%$ in the cosmic ray at 100 TeV (Fig. 6). Therefore, the assumption leads to a maximum of 10% errors in the $K^-/K^+$ ratio. We note that this assumption affects only on the $\nu/\bar{\nu}$ ratio at high energies. We expect almost no effect for the $\nu/\bar{\nu}$ ratio at low energies, because of the proton dominance in the low energy cosmic ray. Also the $\nu+\bar{\nu}$ flux is not affected in any energy region.

The atmospheric $\nu$ fluxes were calculated by integrating those $\nu$-yield functions with the nucleon fluxes shown in Fig. 5:

$$F_\nu(E_\nu) = \int_{E\min}^{E\max} [\eta_\nu^p(E,E_\nu,\theta)F_p(E) + \eta_{\bar{\nu}}^p(E,E_\nu,\theta)F_n(E)]dE \quad (4.8)$$

and

$$F_{\bar{\nu}}(E_\nu) = \int_{E\min}^{E\max} [\eta_{\bar{\nu}}^p(E,E_\nu,\theta)F_p(E) + \eta_\nu^p(E,E_\nu,\theta)F_n(E)]dE\ , \quad (4.9)$$

where $F_\nu(F_{\bar{\nu}})$ is the atmospheric $\nu(\bar{\nu})$ flux, $F_p$ and $F_n$ are the proton and neutron fluxes, respectively, and $\nu$ stands for $\nu_\mu$ or $\nu_e$. We took $E_{\min}$ equal to the $\nu$ energy and $E_{\max} = 1000$ TeV.

The results of the integrations (4.8) and (4.9) are sum-

TABLE V. $\bar{\nu}_\mu$ flux $\times E_\nu^3$ ($\mathrm{m^{-2}\,sec^{-1}\,sr^{-1}\,GeV^2}$) calculated with the hybrid method. The value above $1\times10^4$ is the smooth extension with a power fit.

| $E_\nu$ (GeV)\ $\cos\theta$ | 0.0–0.1 | 0.1–0.2 | 0.2–0.3 | 0.3–0.4 | 0.4–0.5 | 0.5–0.6 | 0.6–0.7 | 0.7–0.8 | 0.8–0.9 | 0.9–1.0 |
|---|---|---|---|---|---|---|---|---|---|---|
| 1.000 | 217.1 | 210.4 | 203.3 | 196.0 | 188.3 | 180.6 | 173.5 | 167.0 | 161.1 | 155.7 |
| 1.259 | 246.6 | 237.4 | 228.0 | 218.4 | 208.7 | 199.1 | 190.4 | 182.6 | 175.7 | 169.6 |
| 1.585 | 274.4 | 262.2 | 249.9 | 237.7 | 225.6 | 213.8 | 203.4 | 194.5 | 186.9 | 180.5 |
| 1.995 | 299.6 | 283.5 | 267.9 | 252.8 | 238.2 | 224.3 | 212.4 | 202.6 | 194.6 | 188.2 |
| 2.512 | 323.6 | 302.6 | 283.2 | 265.0 | 248.2 | 232.7 | 219.7 | 209.2 | 200.9 | 194.6 |
| 3.162 | 348.0 | 321.3 | 297.5 | 276.5 | 257.7 | 241.1 | 227.5 | 216.4 | 207.7 | 201.1 |
| 3.981 | 371.7 | 338.6 | 310.5 | 286.6 | 266.3 | 249.1 | 235.0 | 223.6 | 214.5 | 207.5 |
| 5.012 | 393.4 | 353.9 | 321.5 | 295.0 | 273.4 | 255.9 | 241.6 | 229.9 | 220.5 | 213.2 |
| 6.310 | 412.6 | 366.6 | 330.2 | 301.4 | 278.9 | 261.5 | 247.1 | 235.3 | 225.6 | 218.0 |
| 7.943 | 429.2 | 377.0 | 336.7 | 305.9 | 282.7 | 265.4 | 251.1 | 239.2 | 229.4 | 221.4 |
| 10.00 | 443.5 | 385.1 | 341.2 | 308.4 | 284.5 | 267.3 | 253.2 | 241.2 | 231.2 | 223.0 |
| 12.59 | 455.6 | 391.0 | 343.5 | 308.9 | 284.3 | 267.3 | 253.3 | 241.3 | 231.2 | 222.7 |
| 15.85 | 465.5 | 394.8 | 343.7 | 307.4 | 282.3 | 265.6 | 251.7 | 239.7 | 229.4 | 220.5 |
| 19.95 | 473.2 | 396.2 | 341.8 | 303.9 | 278.4 | 262.1 | 248.5 | 236.5 | 225.9 | 216.6 |
| 25.12 | 478.4 | 395.3 | 337.8 | 298.5 | 272.8 | 257.0 | 243.6 | 231.6 | 220.8 | 211.1 |
| 31.62 | 481.3 | 393.0 | 332.8 | 292.5 | 266.7 | 251.3 | 238.2 | 226.3 | 215.3 | 205.2 |
| 39.81 | 482.1 | 389.9 | 328.0 | 286.9 | 261.2 | 246.1 | 233.3 | 221.4 | 210.3 | 200.0 |
| 50.12 | 480.9 | 386.3 | 323.3 | 281.9 | 256.2 | 241.5 | 228.9 | 217.1 | 206.0 | 195.6 |
| 63.10 | 477.6 | 382.0 | 318.7 | 277.3 | 251.8 | 237.3 | 224.9 | 213.2 | 202.2 | 191.8 |
| 79.43 | 472.2 | 377.1 | 314.2 | 273.2 | 247.9 | 233.5 | 221.3 | 209.8 | 198.9 | 188.7 |
| 100.0 | 464.8 | 371.6 | 309.8 | 269.4 | 244.4 | 230.2 | 218.1 | 206.8 | 196.2 | 186.2 |
| 125.9 | 456.0 | 365.2 | 304.8 | 265.2 | 240.6 | 226.5 | 214.5 | 203.4 | 193.0 | 183.4 |
| 158.5 | 446.2 | 357.5 | 298.4 | 259.6 | 235.4 | 221.5 | 209.7 | 198.8 | 188.7 | 179.3 |
| 199.5 | 435.4 | 348.6 | 290.8 | 252.8 | 229.1 | 215.4 | 203.8 | 193.1 | 183.2 | 174.0 |
| 251.2 | 423.8 | 338.6 | 282.0 | 244.8 | 221.6 | 208.2 | 196.9 | 186.4 | 176.6 | 167.6 |
| 316.2 | 411.5 | 327.7 | 272.1 | 235.7 | 213.2 | 200.1 | 189.1 | 178.8 | 169.2 | 160.3 |
| 398.1 | 398.7 | 316.4 | 262.0 | 226.4 | 204.3 | 191.5 | 180.6 | 170.4 | 160.9 | 152.0 |
| 501.2 | 385.6 | 305.5 | 252.4 | 217.5 | 195.7 | 182.7 | 171.6 | 161.3 | 151.6 | 142.6 |
| 631.0 | 372.3 | 294.9 | 243.2 | 209.1 | 187.2 | 173.8 | 162.3 | 151.6 | 141.7 | 132.5 |
| 794.3 | 358.9 | 284.6 | 234.6 | 201.0 | 179.0 | 164.9 | 152.8 | 141.6 | 131.3 | 121.9 |
| 1000.0 | 345.5 | 274.7 | 226.4 | 193.2 | 170.9 | 156.0 | 143.1 | 131.3 | 120.7 | 110.9 |
| 1259.0 | 331.6 | 264.6 | 217.9 | 185.2 | 162.4 | 146.5 | 132.7 | 120.4 | 109.3 | (99.4) |
| 1585.0 | 317.1 | 253.8 | 208.7 | 176.3 | 153.0 | 136.0 | 121.4 | 108.5 | (97.2) | (87.1) |
| 1995.0 | 302.1 | 242.4 | 198.8 | 166.6 | 142.8 | 124.8 | 109.5 | (96.2) | (84.7) | (74.7) |
| 2512.0 | 286.7 | 230.6 | 188.2 | 156.3 | 132.0 | 113.2 | (97.4) | (83.9) | (72.4) | (62.6) |
| 3162.0 | 278.89 | 210.88 | 165.26 | 134.27 | 113.09 | (98.3) | (85.8) | (74.9) | (65.5) | (57.2) |
| $10^4$ | (206.9) | (133.8) | (92.1) | (67.4) | (52.6) | (43.2) | (35.7) | (29.4) | (24.1) | (19.6) |
| $3.16\times10^4$ | (138.2) | (70.8) | (40.2) | (25.3) | (17.6) | (13.4) | (10.2) | (7.7) | (5.8) | (4.3) |

marized in Tables IV, V, VI, and VII down to 1 GeV. The calculated fluxes below 10 GeV smoothly connect to the low energy calculation at around 3 GeV (Fig. 11). This shows that the systematic difference between the calculations for high energy and low energy atmospheric $\nu$ fluxes (Sec. IV B) is very small. With the limited number of protons used in the calculation of $\nu$-yield functions at high energies, the errors involved in $\{A, B, C\}$ become large due to large fluctuations. Therefore, the error in the flux value increases at high energies. This error is estimated to be $\lesssim 5\%$ for $\nu_\mu$ and $\bar{\nu}_\mu$ below 100 GeV, and increases to 10% at around 3000 GeV for near horizontal directions. The error for $\nu_e$ and $\bar{\nu}_e$ fluxes is larger than $\nu_\mu$ and $\bar{\nu}_\mu$ fluxes; it may exceed 10% at 1000 GeV for near horizontal directions and at 100 GeV for near vertical directions. For $\nu_\mu$'s and $\bar{\nu}_\mu$'s, however, we extrapolate the flux value up to $3.16 \times 10^4$ GeV. We note that large errors at these energies do not affect much the expected flux of upgoing $\mu$'s, because the contribution of $\nu$'s with $E_\nu > 1000$ GeV is estimated to be less than 15%. The value in the parentheses is estimated to have a larger error than 10%.

The $\nu$ fluxes below 3 GeV could differ substantially from the true flux, since solar modulation and geomagnetic effects have not been included. The fluxes for $\leq$ 3 GeV in these tables should be regarded as those for solar mid and low cutoff rigidity ($\lesssim$ 3 GV). They also are depicted for the near vertical and near horizontal directions in Fig. 14 with the results of other authors. The $\nu_\mu(\bar{\nu}_\mu)$ fluxes are almost proportional to $E_\nu^{-3}$ from 1 GeV to 1 TeV. On the other hand, the $\nu_e(\bar{\nu}_e)$ fluxes decrease, being proportional to $E_\nu^{-3.5}$ or steeper above 10 GeV. Our $\nu_\mu$ flux for near horizontal directions agrees with that of Volkova [12] and Lipari [15] above 10 GeV to within $\sim$ 5%. For near vertical directions, our calculation is 10–15 % larger than that of Volkova and Mitsui *et al.* [13], and by 5–10 % than that of Lipari. For $\nu_e$ fluxes, our calculation is larger than others by 10–20 % above 10 GeV for both directions.

If we take the lower line for the extrapolation of the proton flux in Fig. 5 for $\geq$ 40 TeV, the $\nu_\mu$ and $\bar{\nu}_\mu$ fluxes decrease $\sim$ 10% at 3000 GeV, but they decrease only a few percent at 1000 GeV. Even if we reduce the upper end of the integrations ($E_{\max}$) to 100 TeV in (4.8) and (4.9), i.e., if there was a sharp cutoff of the cosmic ray spectrum at 1000 TeV, the $\nu_\mu$ and $\bar{\nu}_\mu$ fluxes are reduced by only $\sim$10% at 1000 GeV. Therefore, even if the cosmic ray composition above 100 TeV is quite different from

TABLE VI. $\nu_e$ flux $\times E_\nu^3$ ($m^{-2}\,sec^{-1}\,sr^{-1}\,GeV^2$) calculated with the hybrid method.

| $E_\nu$ (GeV)\ $\cos\theta$ | 0.0–0.1 | 0.1–0.2 | 0.2–0.3 | 0.3–0.4 | 0.4–0.5 | 0.5–0.6 | 0.6–0.7 | 0.7–0.8 | 0.8–0.9 | 0.9–1.0 |
|---|---|---|---|---|---|---|---|---|---|---|
| 1.000 | 131.2 | 124.3 | 116.7 | 109.0 | 101.3 | 94.0 | 87.2 | 81.0 | 75.6 | 70.9 |
| 1.259 | 150.9 | 140.8 | 130.5 | 120.4 | 110.7 | 101.7 | 93.6 | 86.4 | 80.2 | 74.9 |
| 1.585 | 166.3 | 154.8 | 142.2 | 129.5 | 117.2 | 105.9 | 95.9 | 87.4 | 80.4 | 75.0 |
| 1.995 | 179.2 | 165.4 | 150.1 | 134.7 | 120.1 | 106.9 | 95.5 | 86.0 | 78.6 | 73.1 |
| 2.512 | 192.5 | 172.0 | 152.6 | 134.9 | 119.1 | 105.5 | 94.0 | 84.6 | 77.1 | 71.3 |
| 3.162 | 205.4 | 176.7 | 152.7 | 132.7 | 116.2 | 102.5 | 91.2 | 81.9 | 74.4 | 68.4 |
| 3.981 | 216.8 | 181.7 | 153.6 | 131.1 | 113.0 | 98.4 | 86.6 | 77.1 | 69.4 | 63.2 |
| 5.012 | 226.2 | 186.9 | 155.3 | 129.9 | 109.7 | 93.5 | 80.7 | 70.5 | 62.5 | 56.3 |
| 6.310 | 233.6 | 190.4 | 155.5 | 127.5 | 105.3 | 87.8 | 74.2 | 63.7 | 55.6 | 49.7 |
| 7.943 | 239.0 | 190.2 | 151.9 | 122.1 | 99.1 | 81.4 | 67.9 | 57.6 | 50.0 | 44.3 |
| 10.00 | 242.3 | 186.2 | 144.9 | 114.2 | 91.5 | 74.5 | 61.8 | 52.3 | 45.3 | 40.1 |
| 12.59 | 243.5 | 178.8 | 134.8 | 104.3 | 82.8 | 67.3 | 55.9 | 47.6 | 41.4 | 36.8 |
| 15.85 | 242.5 | 168.3 | 122.5 | 93.0 | 73.4 | 59.9 | 50.4 | 43.4 | 38.2 | 34.1 |
| 19.95 | 239.1 | 156.4 | 109.8 | 82.0 | 64.6 | 53.1 | 45.3 | 39.7 | 35.4 | 31.8 |
| 25.12 | 233.3 | 144.7 | 98.4 | 72.4 | 56.9 | 47.2 | 40.8 | 36.2 | 32.7 | 29.5 |
| 31.62 | 225.2 | 133.1 | 88.0 | 63.9 | 50.2 | 42.0 | 36.7 | 33.0 | 30.1 | 27.3 |
| 39.81 | 215.2 | 121.9 | 78.6 | 56.5 | 44.4 | 37.4 | 33.1 | 30.1 | 27.6 | 25.1 |
| 50.12 | 203.6 | 111.2 | 70.2 | 50.1 | 39.5 | 33.5 | 29.9 | 27.5 | 25.3 | 22.9 |
| 63.10 | 190.7 | 100.9 | 62.7 | 44.5 | 35.1 | 30.0 | 27.1 | 25.0 | 23.1 | 20.7 |
| 79.43 | 176.8 | 91.3 | 56.0 | 39.6 | 31.4 | 27.0 | 24.5 | 22.8 | 21.0 | 18.7 |
| 100.0 | 162.3 | 82.2 | 50.0 | 35.3 | 28.1 | 24.3 | 22.2 | 20.7 | 19.0 | 16.7 |
| 125.9 | 147.4 | 73.6 | 44.6 | 31.5 | 25.2 | 22.0 | 20.2 | 18.8 | 17.2 | 14.9 |
| 158.5 | 132.6 | 65.7 | 39.7 | 28.2 | 22.7 | 19.9 | 18.3 | 17.1 | 15.5 | 13.1 |
| 199.5 | 118.1 | 58.4 | 35.4 | 25.3 | 20.5 | 18.1 | 16.7 | 15.5 | 13.9 | (11.5) |
| 251.2 | 104.1 | 51.7 | 31.6 | 22.8 | 18.6 | 16.5 | 15.2 | 14.0 | 12.4 | (10.0) |
| 316.2 | 90.9 | 45.5 | 28.1 | 20.5 | 16.9 | 15.1 | 13.9 | 12.7 | (11.0) | (8.7) |
| 398.1 | 78.5 | 39.9 | 25.0 | 18.5 | 15.4 | 13.8 | 12.7 | (11.5) | (9.8) | (7.5) |
| 501.2 | 67.1 | 34.9 | 22.3 | 16.7 | 14.1 | (12.7) | (11.6) | (10.4) | (8.7) | (6.4) |
| 631.0 | 56.8 | 30.3 | 19.8 | 15.1 | 12.9 | (11.6) | (10.6) | (9.4) | (7.6) | (5.4) |
| 794.3 | 47.6 | 26.2 | 17.6 | 13.7 | (11.8) | (10.7) | (9.8) | (8.5) | (6.7) | (4.6) |
| 1000.0 | 39.5 | 22.6 | 15.7 | 12.5 | (10.9) | (9.9) | (9.0) | (7.7) | (5.9) | (3.8) |

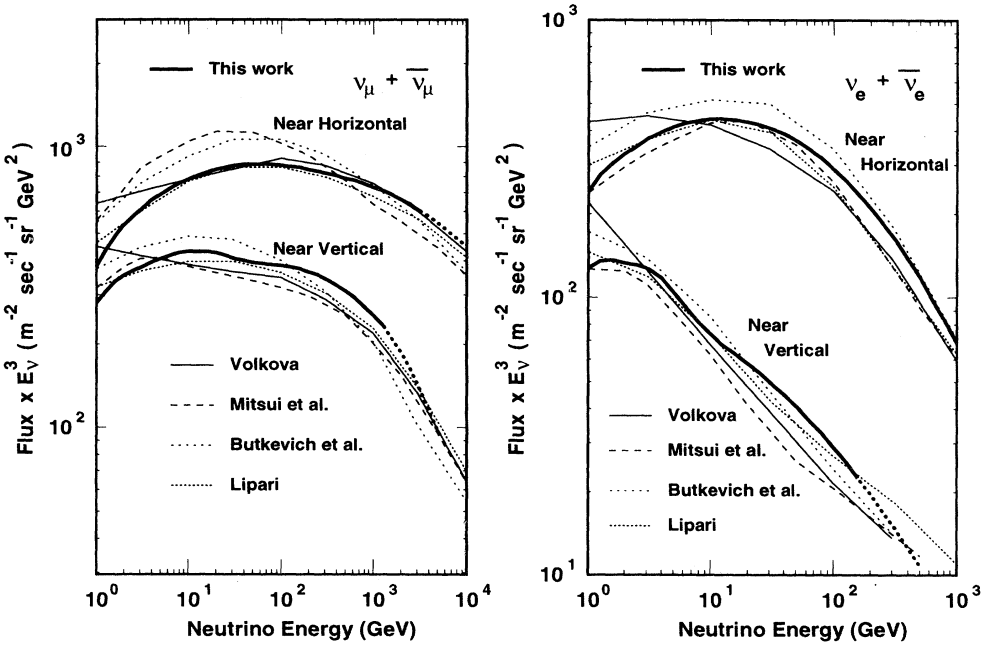


FIG. 14. $\nu_\mu + \bar{\nu}_\mu$ and $\nu_e + \bar{\nu}_e$ fluxes for near horizontal ($\cos\theta$= 0–0.1) and near vertical ($\cos\theta$= 0.9–1.0) directions. Volkova is from Ref. [12], Mitsui *et al.* from Ref. [13], Butkevich *et al.* from Ref. [14], and Lipari from Ref. [15]. We used the fluxes of $\cos\theta = 0.05$ for near horizontal and $\cos\theta = 1$ for near vertical directions of Volkova and Lipari, those of $\theta_{\rm zenith} = 87°$ for near horizontal and $\theta_{\rm zenith} = 0$ for near vertical directions of Mitsui *et al.*, and those of $\cos\theta = 0$ for near horizontal and $\cos\theta = 1$ for near vertical directions of Butkevich *et al.*

TABLE VII. $\bar{\nu}_e$ flux $\times E_\nu^3$ ($m^{-2}\,sec^{-1}\,sr^{-1}\,GeV^2$) calculated with the hybrid method.

| $E_\nu$ (GeV)\ $\cos\theta$ | 0.0–0.1 | 0.1–0.2 | 0.2–0.3 | 0.3–0.4 | 0.4–0.5 | 0.5–0.6 | 0.6–0.7 | 0.7–0.8 | 0.8–0.9 | 0.9–1.0 |
|---|---|---|---|---|---|---|---|---|---|---|
| 1.000 | 109.2 | 103.1 | 96.5 | 89.8 | 83.2 | 77.0 | 71.1 | 65.9 | 61.3 | 57.3 |
| 1.259 | 126.1 | 117.3 | 108.3 | 99.6 | 91.4 | 83.7 | 76.8 | 70.7 | 65.4 | 61.0 |
| 1.585 | 139.2 | 129.2 | 118.4 | 107.5 | 97.1 | 87.5 | 79.1 | 71.9 | 66.1 | 61.5 |
| 1.995 | 149.9 | 138.1 | 125.1 | 112.0 | 99.7 | 88.7 | 79.1 | 71.2 | 65.0 | 60.5 |
| 2.512 | 160.7 | 143.4 | 127.1 | 112.2 | 99.1 | 87.8 | 78.3 | 70.5 | 64.3 | 59.6 |
| 3.162 | 170.7 | 146.7 | 126.8 | 110.3 | 96.7 | 85.4 | 76.2 | 68.7 | 62.6 | 57.8 |
| 3.981 | 179.2 | 150.2 | 127.2 | 108.8 | 94.1 | 82.2 | 72.7 | 65.0 | 58.8 | 53.9 |
| 5.012 | 186.0 | 154.0 | 128.3 | 107.8 | 91.3 | 78.2 | 67.9 | 59.7 | 53.3 | 48.3 |
| 6.310 | 191.2 | 156.4 | 128.2 | 105.7 | 87.7 | 73.6 | 62.5 | 54.0 | 47.5 | 42.7 |
| 7.943 | 194.8 | 155.8 | 125.1 | 101.2 | 82.6 | 68.3 | 57.3 | 48.9 | 42.7 | 38.2 |
| 10.00 | 196.8 | 152.3 | 119.2 | 94.6 | 76.2 | 62.5 | 52.1 | 44.4 | 38.6 | 34.4 |
| 12.59 | 197.1 | 146.0 | 111.0 | 86.5 | 69.0 | 56.4 | 47.2 | 40.3 | 35.2 | 31.3 |
| 15.85 | 195.8 | 137.3 | 100.8 | 77.1 | 61.3 | 50.3 | 42.4 | 36.6 | 32.2 | 28.8 |
| 19.95 | 192.6 | 127.6 | 90.4 | 68.1 | 53.9 | 44.5 | 38.0 | 33.3 | 29.6 | 26.5 |
| 25.12 | 187.6 | 118.0 | 81.1 | 60.1 | 47.5 | 39.5 | 34.1 | 30.2 | 27.0 | 24.2 |
| 31.62 | 180.9 | 108.6 | 72.6 | 53.2 | 42.0 | 35.1 | 30.6 | 27.3 | 24.6 | 21.9 |
| 39.81 | 172.6 | 99.5 | 65.0 | 47.1 | 37.1 | 31.2 | 27.4 | 24.7 | 22.3 | 19.7 |
| 50.12 | 163.0 | 90.6 | 58.0 | 41.7 | 32.9 | 27.8 | 24.6 | 22.2 | 20.1 | 17.7 |
| 63.10 | 152.3 | 82.1 | 51.6 | 36.9 | 29.1 | 24.7 | 22.0 | 20.0 | 18.1 | 15.7 |
| 79.43 | 140.8 | 74.0 | 45.9 | 32.6 | 25.8 | 22.1 | 19.8 | 18.0 | 16.2 | 13.9 |
| 100.0 | 128.8 | 66.3 | 40.7 | 28.9 | 22.9 | 19.7 | 17.7 | 16.1 | 14.4 | 12.3 |
| 125.9 | 116.5 | 59.0 | 36.0 | 25.5 | 20.3 | 17.6 | 15.9 | 14.5 | 12.8 | (10.7) |
| 158.5 | 104.4 | 52.3 | 31.8 | 22.6 | 18.1 | 15.7 | 14.2 | 12.9 | 11.4 | (9.4) |
| 199.5 | 92.5 | 46.1 | 28.0 | 20.0 | 16.1 | 14.0 | 12.7 | 11.5 | (10.1) | (8.1) |
| 251.2 | 81.1 | 40.3 | 24.6 | 17.7 | 14.3 | 12.5 | 11.4 | (10.3) | (8.9) | (7.0) |
| 316.2 | 70.3 | 35.1 | 21.6 | 15.6 | 12.7 | 11.2 | (10.2) | (9.1) | (7.8) | (6.0) |
| 398.1 | 60.3 | 30.4 | 18.9 | 13.8 | 11.3 | (10.0) | (9.1) | (8.1) | (6.8) | (5.1) |
| 501.2 | 51.2 | 26.2 | 16.5 | 12.2 | (10.1) | (9.0) | (8.1) | (7.2) | (5.9) | (4.3) |
| 631.0 | 43.0 | 22.4 | 14.4 | (10.8) | (9.0) | (8.0) | (7.3) | (6.4) | (5.1) | (3.6) |
| 794.3 | 35.8 | 19.1 | 12.5 | (9.5) | (8.0) | (7.2) | (6.5) | (5.6) | (4.4) | (3.0) |
| 1000.0 | 29.4 | 16.2 | (10.8) | (8.4) | (7.2) | (6.4) | (5.8) | (4.9) | (3.8) | (2.5) |

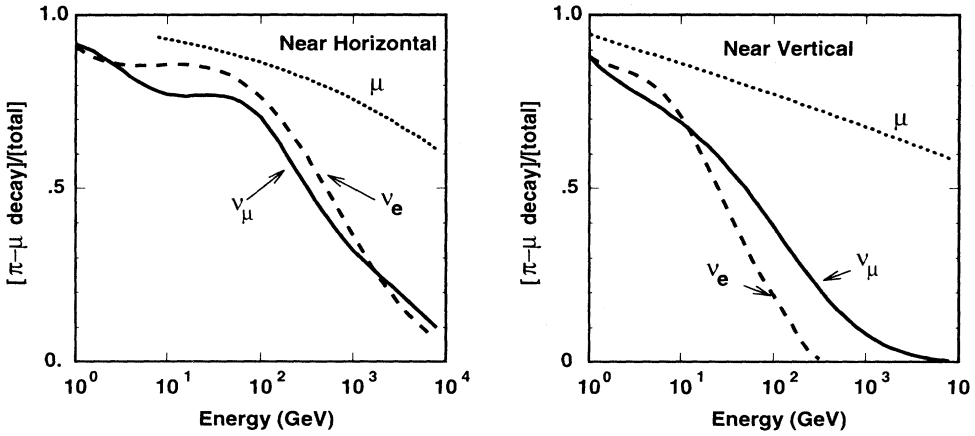


FIG. 15. The ratio of $\nu_\mu+\bar{\nu}_\mu$, $\nu_e+\bar{\nu}_e$, and $\mu^+ + \mu^-$ fluxes produced by $\pi$-$\mu$ decay to the total fluxes. Solid lines show that for $\nu_\mu + \bar{\nu}_\mu$, dashed lines for $\nu_e + \bar{\nu}_e$, and dotted lines for $\mu^+ + \mu^-$. Near horizontal denotes the average over $\cos\theta$= 0–0.1 and near vertical denotes that over $\cos\theta$= 0.9–1.

our assumption, our calculation does not give a different result for the atmospheric $\nu$ fluxes below 1000 GeV by more than 10%. However, for the accurate calculation of atmospheric $\nu$'s above 1000 GeV, it is necessary to determine the flux and composition of primary cosmic rays above 1000 TeV per nucleon accurately.

To study the portions of $\nu$'s resulting from $K$'s and from $\pi$-$\mu$ decay, we also calculated the $\nu$ fluxes produced only with $\pi$-$\mu$ decay and show the ratio to the total flux in Fig. 15. The contribution of charmed mesons to atmospheric $\nu$'s is very small in this energy range. The $\mu$ flux which resulted from $\pi$ decay was also calculated and the ratio to the total flux is also shown in the same figure. It is seen that the $\nu$'s created by $\pi$-$\mu$ decay are the minor component above $\sim$ 30 GeV for near vertical directions and $\sim$ 500 GeV for near horizontal directions both for $\nu_\mu$'s and $\nu_e$'s. It is also seen that although the main source of $\mu$ fluxes is $\pi$ decay up to 10 000 GeV, the main source of atmospheric $\nu$'s is $K$'s above $\sim$ 30 GeV for near vertical directions and above $\sim$ 500 GeV for near horizontal directions.

The ratios $\nu_\mu/\bar{\nu}_\mu$ and $\nu_e/\bar{\nu}_e$ are shown in in Figs. 16 and 17 for near vertical and near horizontal directions with results of other authors. It is difficult to determine the ratio accurately with the Monte Carlo method, especially near the high energy end. We do not consider the variation of $\sim$ 0.05 for each ratio to be meaningful. Also the assumption (4.7) is the source of errors in the $\nu_\mu/\bar{\nu}_\mu$ and $\nu_e/\bar{\nu}_e$ ratios at high energies, since the main source of atmospheric $\nu$'s is the $K$ decay. However, the $\nu_\mu/\bar{\nu}_\mu$ ratio is clearly smaller than other calculations [14,15], especially for near vertical directions even in the energy region where the assumption (4.7) is good ($\lesssim$ 30 GeV). For the $\nu_e/\bar{\nu}_e$ ratio, the agreement with other calculations is better than the $\nu_\mu/\bar{\nu}_\mu$ ratio, but also shows significant differences at $E_\nu < 30$ GeV for near vertical directions. Since we have sufficient statistics at $E_\nu < 30$ GeV both for $\nu_\mu$ and $\nu_e$ in our Monte Carlo method, we consider that those differences result from differences in the calculation schemes, such as the interaction model and/or the atmospheric density structure. Our ratios calculated here agree well with those calculated in Sec. IV B at $\sim$ 3 GeV.

The ratio $(\nu_\mu+\bar{\nu}_\mu)/(\nu_e+\bar{\nu}_e)$ calculated here is also compared with other authors in Fig. 18. Our result is smaller than others for $\gtrsim$ 10 GeV both for near vertical and near horizontal directions, reflecting the larger $\nu_e$ fluxes than

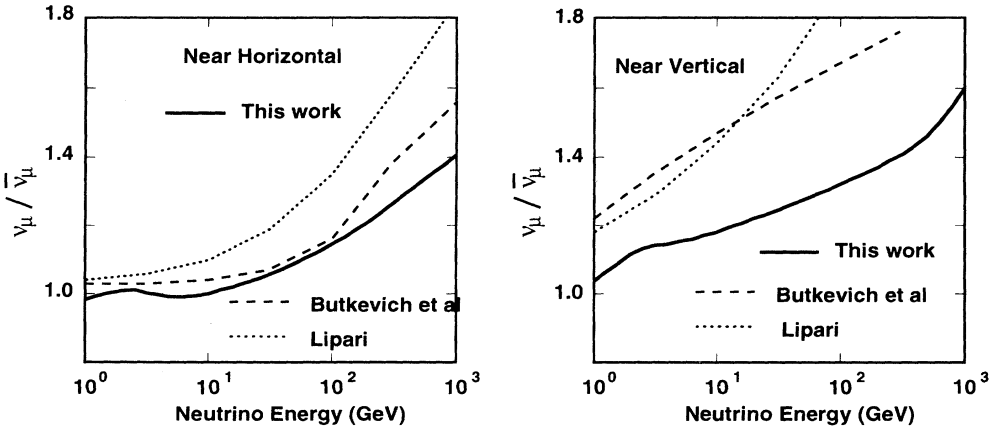


FIG. 16. $\nu_\mu/\bar{\nu}_\mu$ ratio. Notation is the same as Fig. 14.

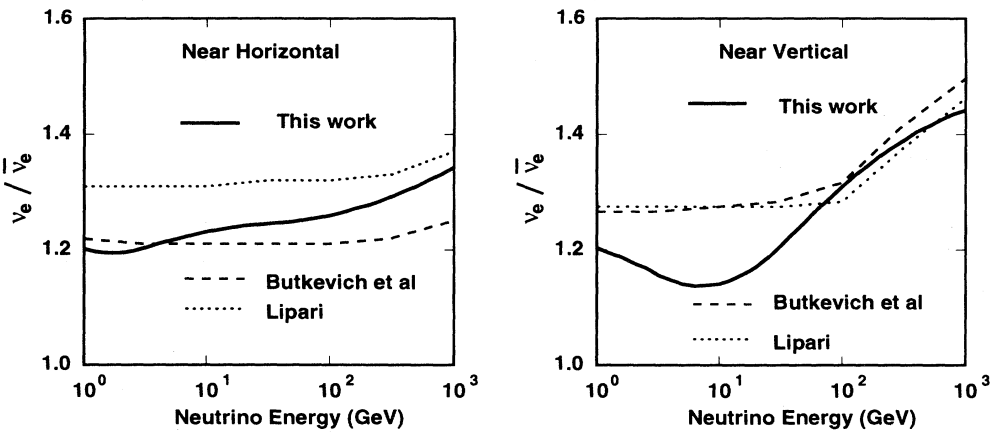


FIG. 17. $\nu_e/\bar{\nu}_e$ ratio. Notation is the same as Fig. 14.

other calculations in this energy region. This may be due to differences in the calculation scheme. However, all results show good agreement in the $\lesssim 10$ GeV region, except for that of Mitsui *et al.* for near horizontal directions. Their result is larger than others by $\sim 50\%$ in the $\lesssim 10$ GeV for near horizontal directions, and by 10–15 % even for near vertical directions in the same energy region. We note that Mitsui *et al.* did not take into account the effect of muon polarization. This explains the difference for near vertical directions, but not for near horizontal directions. There seems to be other differences in their calculation scheme.

### D. Flux of atmospheric muons

There have been many observations of $\mu$ flux for near vertical and near horizontal directions at sea level. Since the $\mu$ flux is the complementary part of the $\nu$ flux in $\pi$-$\mu$ decay, the calculation of $\nu$ fluxes is often examined by the comparison of the calculated $\mu$ flux with the observed flux. We calculated the atmospheric $\mu$ flux using the hybrid method; we first calculate the $\mu$-yield function, then integrate it with the nucleon flux. In Fig. 19, we present our calculated $\mu^+ + \mu^-$ fluxes for near vertical directions ($\cos\theta = 0.9$–1) and the observed near vertical flux, and in Fig. 20 for near horizontal directions. We note that although the main source is different mesons for atmospheric $\mu$'s and $\nu$'s at high energies, the nucleon energy dependence of the $\mu$-yield function is very similar to that of the $\nu_\mu$ flux above 100 GeV for all zenith angles.

In the same figures, we show the calculated results of Butkevich *et al.* [14] and Lipari [15]. We used the result of $\cos\theta = 1$ for the near vertical direction and of $\cos\theta = 0$ for near horizontal directions for these authors. Since the

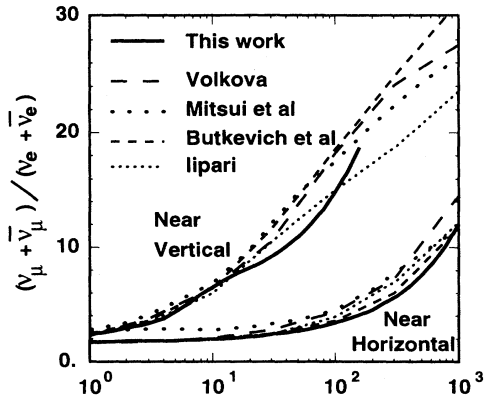


FIG. 18. $(\nu_\mu + \bar{\nu}_\mu)/(\nu_e + \bar{\nu}_e)$-ratio. Notation is the same as Fig. 14.

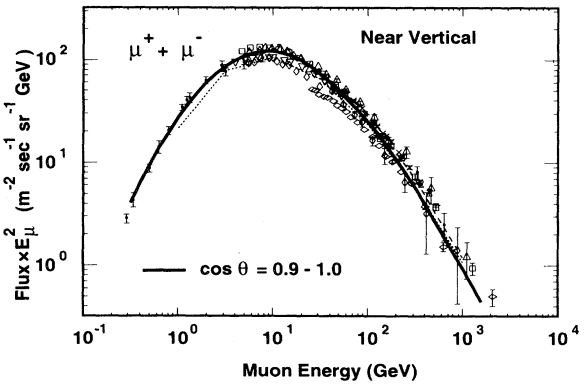


FIG. 19. Calculated $\mu^+ + \mu^-$ flux for $\cos\theta = 0.9$–1 and observed fluxes. Dots are from Ref. [62], squares from Ref. [63], crosses from Ref. [64], minuses from Ref. [65], upward triangles from Ref. [66], downward triangles from Ref. [67], vertical diamonds from Ref. [68], and horizontal diamonds from Ref. [69]. Also shown are the calculated results from Ref. [14] (dashed thin line) and Ref. [15] (dotted thin line) both for $\cos\theta = 1$.

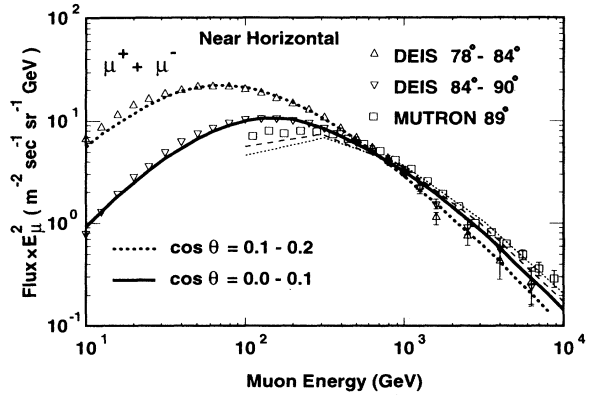


FIG. 20. Calculated $\mu^+ + \mu^-$ flux for $\cos\theta = 0$–0.1 (solid line) and 0.1–0.2 (dotted line), and the observed flux by the DEIS [69] and MUTRON [70] groups. Also shown are calculated results from Ref. [14] (dashed thin line) and Ref. [15] (dotted thin line) both for $\cos\theta = 0$, for comparison with the MUTRON data. We note that the DEIS observation is added for the zenith angle bins of 78°–84° and 84°–90° corresponding to $\cos\theta = 0.1$–0.2 and $\cos\theta = 0$–0.1.

DEIS group measured the $\mu$ flux at many zenith angles, we summed their data in zenith angle bins of 78°–84° and 84°–90° corresponding to $\cos\theta = 0.1$–0.2 and $\cos\theta = 0$–0.1. The MUTRON group measured the muon flux in the direction of 86°–90° and the flux-averaged zenith angle is 89°.

It can be seen that the agreement of our calculation and the observations is good, although there is some variation in observed fluxes among the different groups. Our calculation agrees with DEIS data within $\sim 15\%$ at all energies and $\lesssim 5\%$ for 100–1000 GeV. The agreement is especially good for the near horizontal directions. Taking into account the fact that average zenith angle of the MUTRON data is 89°, the agreement of MUTRON data and our calculation is also very good. However, since the main parent mesons are different for $\nu$'s and $\mu$'s, these agreements shown above do not fully justify our calculation of $\nu$ fluxes.

The charge ratio $\mu^+/\mu^-$ was also calculated and is shown in Fig. 21 with the result of other authors [14,15]. As we do not consider the variation of $\lesssim 0.05$ to be meaningful in our calculation, a constant value of $\sim 1.25$ can explain our results both for near vertical and near horizontal directions. Other calculations show an increase with energy, especially for the near vertical directions. We note that the assumption (4.7) is almost valid for $\mu^+/\mu^-$ ratio, since the main source is still the $\pi$-$\mu$ decay, and the experimental results do not show such an increase but are consistent with the constant value $\sim 1.25$ for both directions.

At low energies, the production altitude of $\nu$'s is 80–300 g/cm$^2$ for vertical directions, which corresponds to 9–18 km (Fig. 22) altitude. Since $\mu$'s travel $\sim 6$ km before decay at 1 GeV on average, $\mu$'s observed at sea level are not directly related to $\nu$'s at low energies ($\lesssim 1$ GeV). For the examination of the calculated atmospheric $\nu$ flux at low energies, the observation of $\mu$ fluxes at the production height is necessary.

Recently, the $\mu^-$ flux has been measured with good accuracy by the MASS (Matter-Antimatter Superconducting Spectrometer) experiment [76] at high altitudes. In Fig. 23, we compared the observed $\mu^-$ fluxes and our calculation at the same altitudes. This $\mu$ flux was calculated by the full Monte Carlo method, the same as the low energy $\nu$ flux. The agreement of experiment and calculation is very good except for very high altitudes ($\lesssim 37$ g/cm$^2$) and the low momentum region at low altitudes (615 g/cm$^2$). We note that since the low energy atmospheric $\nu$'s are created at the altitude of 80–300 g/cm$^2$, the contribution of atmospheric $\nu$'s created at very high altitude ($\lesssim 37$ g/cm$^2$) or low altitude (615 g/cm$^2$) to the total $\nu$ flux is relatively small. (See Fig. 22.)

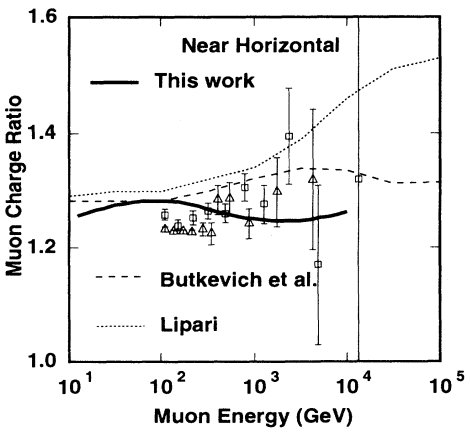


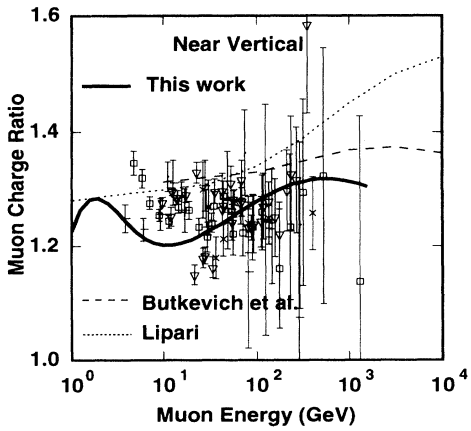


FIG. 21. Comparison of calculated $\mu^+/\mu^-$ ratios with observations. For the near vertical directions, dots are from Ref. [62], crosses from Ref. [69], squares from Ref. [72], minuses from Ref. [73], upward triangles from Ref. [74], and diamonds from Ref. [75]. For the near horizontal directions, triangles are Ref. [70] and squares from Ref. [71]. Also for the near horizontal direction, calculated $\mu^+/\mu^-$ ratios are averaged for $\cos\theta = 0 - 0.2$ for the results of Lipari and this work.

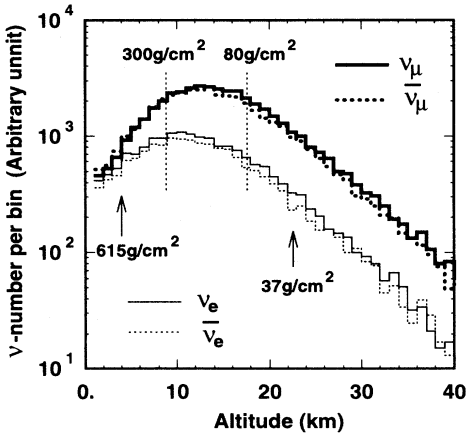


FIG. 22. Production height distribution of $\nu$'s with energy $\geq$ 400 MeV by vertical cosmic rays.

## V. SYSTEMATIC ERROR AND OTHER UNCERTAINTIES

The systematic error in the atmospheric $\nu$ fluxes comes mainly from the uncertainty of the cosmic ray primary flux. Even at low energies, where the primary cosmic ray flux is rather well studied, it is difficult to determine the absolute value due to the uncertainties in the instrumental efficiency ($\sim$ 12%) and exposure factor (2–3 %) [31]. These uncertainties in the primary cosmic ray flux increase with energy. In our compilation, the error in the fit is $\sim$ 10% for the nucleon flux at 100 GeV and $\sim$ 20% at 100 TeV. Assuming $\sim$ 10% uncertainty below 100 GeV, the systematic error in the atmospheric $\nu$ fluxes is estimated to be $\sim$ 10% at $\leq$ 3 GeV, increasing to $\sim$ 20% at 100 GeV, and remaining almost constant up to 1000 GeV.

We note that the uncertainty of the primary cosmic ray flux increases more rapidly than the fitting error above 10 TeV/nucleon. The JACEE group suggests a steepening of the cosmic ray proton spectrum above 40 TeV [34]. Using this steep proton spectrum, the atmospheric $\nu$ flux decreases 3–4 % at 1000 GeV, $\sim$ 10% at 3000 GeV, and $\gtrsim$ 20% above 10 000 GeV. Below 300 GeV, the difference is negligibly small.

The uncertainty in the nucleon spectrum above 100 TeV, where almost no direct observations are available, is crucial for the calculation of atmospheric $\nu$'s above 1000 GeV. The air shower technique, which is commonly used to study cosmic rays above 100 TeV, cannot determine the chemical composition with the accuracy we need. The nucleon spectrum could be very different from that assumed here, depending on the major chemical component of cosmic rays above 100 TeV.

The interaction model is another source of systematic errors. In our comparison, the agreement of the LUND model and the COSMOS code with the experimental data is $\lesssim$ 10%. The agreement of the NUCRIN code and experimental data is not as good as the LUND code. The authors of the NUCRIN code claim that the agreement is within 10–20 % [47]. However, the hadronic interaction below 5 GeV is related to very low energy atmospheric $\nu$ fluxes; when we switch off the hadronic interaction for $\leq$ 5 GeV, they decrease 2–5 % at 1 GeV, 15–25 % at 300 MeV, and 45–55 % at 100 MeV depending on the rigidity cutoff. Therefore, we may conclude that the error of the NUCRIN code does not affect the atmospheric $\nu$ flux by more than 10% in our calculation for $\geq$ 300 MeV. The systematic error caused by the hadronic interaction model is estimated to be $\sim$ 10% above 300 MeV.

The calculation scheme, the one-dimensional approximation in all energy regions and the superposition model for nucleus-nucleus interactions at high energies, is also the possible source of some systematic error. Since the one-dimensional approximation is justified at high energies, it is expected to be accurate above 3 GeV. With the one-dimensional approximation, however, the calculation of rigidity cutoff is very simplified, and this may result in a systematic error in the absolute value of the atmospheric $\nu$ fluxes of 10–20 % at 100 MeV and 5% at 1 GeV. Other effects caused by the one-dimensional approximation and errors due to the superposition model at high energies are considered to be small compared to other errors.

The calculation method also results in an error in the atmospheric $\nu$ flux. With the full Monte Carlo calculation, it is estimated to be

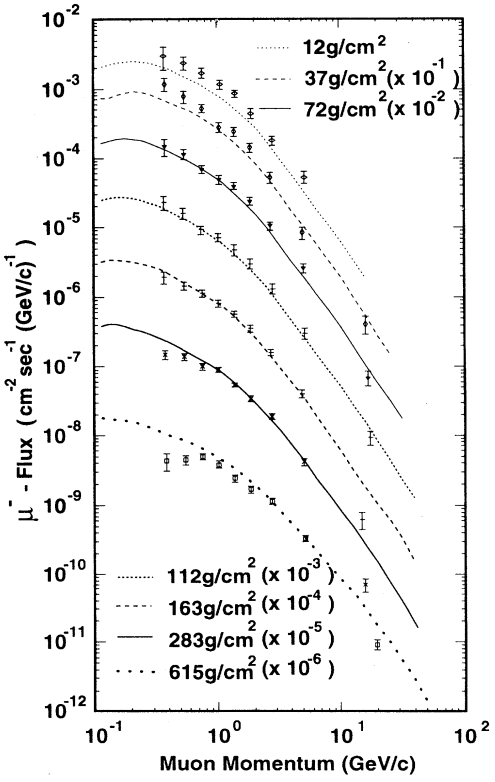


FIG. 23. A comparison of $\mu^-$ fluxes observed by the MASS (Matter-Antimatter Superconducting Spectrometer) experiment [76] at several altitudes and this work.

$\lesssim$2–3 % for 30 MeV to 3 GeV due to the statistics. With the hybrid method, the statistics and the fitting error are sources of the uncertainty. Both the statistics and fitting error are combined and estimated to be $\lesssim$ 5% up to 100–300 GeV for $\nu_\mu$ and $\bar{\nu}_\mu$, and up to 30–100 GeV for $\nu_e$ and $\bar{\nu}_e$, depending on the zenith angle.

Combining all the systematic and nonsystematic errors, the total error is estimated as 20% at 100 MeV, 15% from 1 to 100 GeV, and 20–25 % at the highest energy in our calculation. However, the errors of the species ratio are smaller than the absolute value, since the $\nu$-species ratio is not affected much by the uncertainty of primary fluxes and the calculation scheme. It is estimated to be $\lesssim$ 10% below 100 GeV for $\nu/\bar{\nu}$ and $\lesssim$ 5% below 30 GeV for $(\nu_\mu + \bar{\nu}_\mu)/(\nu_e + \bar{\nu}_e)$. These errors also increase to 10–15 % at the highest energies in our calculation.

Although the main parent meson is different for high energy atmospheric $\mu$'s and $\nu$'s, one may consider that the comparison of calculated and observed atmospheric $\mu$ flux reduces the systematic error due to the primary cosmic ray flux. The agreement of our calculation, DEIS data, and MUTRON data for near horizontal directions (Fig. 20) suggests that the systematic error of the atmospheric $\nu$ flux caused by the uncertainty of the cosmic ray flux may be $\lesssim$ 10% at $E_\nu$ = 100–1000 GeV in our calculation. However, we note that there are similar problems for observation of $\mu$ fluxes with that of primary cosmic rays: determining the instrumental efficiency and the exposure factor. The MASS group claims that their total uncertainty in efficiency is around 20%. This systematic error for ground-based experiments could be smaller, but it is seen in Fig. 19 that $\mu$ fluxes observed for near vertical directions by different groups differ by more than 20%. Also taking the possible systematic error in the $K/\pi$ ratio into account, we conclude that the systematic error caused by the uncertainty in the primary flux is $\sim$ 20% at $E_\nu$ = 1000 GeV.

## VI. SUMMARY

In this paper, we presented the calculation of atmospheric $\nu$ fluxes as follows. First, we summarized the physics related to the primary cosmic ray flux. The low energy cosmic ray flux was parametrized following the work of Nagashima *et al.* [32] based on the compilation of the cosmic ray spectrum by Webber and Lezniak [22] for solar max, mid, and min. In order to calculate the rigidity cutoff due to the geomagnetic field, we simulated the trajectories of cosmic rays. Also the primary cosmic ray flux in the 100 GeV to 100 TeV range was compiled for H, He, CNO, Ne-S, and Fe nuclei groups calculating the nucleon flux for protons and neutrons. We used the NUCRIN interaction model [46,47] for $<$ 5 GeV, LUND model (JETSET version 6.3) [48,49] for 5–500 GeV, and COSMOS for $>$ 500 GeV for the hadronic interactions of cosmic rays. The atmospheric $\nu$ flux was calculated with a full Monte Carlo method for 30 MeV to 3 GeV and with a hybrid method for 1–1000 GeV.

One of the most important results for low energy $\nu$ fluxes is that the ratio $(\nu_e + \bar{\nu}_e)/(\nu_\mu + \bar{\nu}_\mu)$ is almost the same ($\sim$ 0.5) as other calculations for 100 MeV to 3 GeV [17–19,21], whereas underground detectors found a significant difference in the ratio ($e$-like event)/($\mu$-like event) from the value expected from the calculated atmospheric $\nu$ flux. We note that the quantity $(\nu_e + \bar{\nu}_e)/(\nu_\mu + \bar{\nu}_\mu)$ remains relatively unaffected by variations in the interaction model and primary cosmic ray spectrum including the chemical composition. The difference between the observed and the expected value of the ratio ($e$-like event)/($\mu$-like event) might be explained by other physics, such as $\nu$ oscillations.

If this difference is to be explained by $\nu$ oscillations with $\Delta m^2 \sim 10^{-2}$ eV$^2$, the upgoing $\mu$-flux, which is induced by the high energy $\nu$-flux, will show a different zenith angle dependence from the expected one. We calculated the zenith angle dependence of the atmospheric $\nu$ flux in detail: for each zenith angle bin of cos $\theta$= 0–0.1, 0.1–0.2, ..., 0.9–1.0, for 1–1000 GeV. This atmospheric $\nu$ flux could be used to calculate the expectation flux of upgoing $\mu$'s. We note that the absolute value and the ratio are connected to the lower values smoothly at $\sim$ 3 GeV. Also they are compared with the calculation of other authors [12–15].

Atmospheric $\mu$ fluxes were also calculated at sea level and at high altitudes. They were compared with the experimental data and the agreements are found to be satisfactory. The agreement at high altitude is especially important for the calculation of the atmospheric $\nu$ flux at low energies. Although the parent mesons are different for atmospheric $\nu$'s and $\mu$'s, our calculation, DEIS data, and MUTRON data agree very well with each other for the $\mu$ flux of near horizontal directions at high energies ($\gtrsim$ 100 GeV). We conclude that we have used a reasonable primary cosmic ray spectrum, chemical composition, and interaction model.

We stress again that the main source of the systematic error in the atmospheric $\nu$ flux is the uncertainty of the primary cosmic ray flux. Especially for the calculation of the atmospheric $\nu$ flux above 1000 GeV, the lack of knowledge of the cosmic ray flux above 100 TeV/nucleon is crucial.

## ACKNOWLEDGMENTS

We are grateful to P.G. Edwards for his careful reading of the manuscript and comments. The numerical calculation were performed the FACOM M780 in the computer room of the Institute for Nuclear Study, University of Tokyo.

[1] K.S. Hirata *et al.*, Phys. Lett. B **205**, 416 (1988); B **280**, 146 (1992).
[2] D. Casper *et al.*, Phys. Rev. Lett. **66**, 2561 (1991); R. Becker-Szendy *et al.*, Phys. Rev. D **66**, 2561 (1991).
[3] P. Litchfield *et al.*, in *Proceedings of International Workshop on $\nu_\mu/\nu_e$ Problem in Atmospheric Neutrinos*, L'Aquila, Italy, 1993, edited by V. Berezinsky and G. Fiorentini (Laboratori Nazionali Del Gran Sasso, Gran Sasso, 1993), p. 114; M.C. Goodman, in *Cosmic Ray Conference*, Proceedings of the Twenty Third International Conference, Calgary, Canada, 1993, edited by R.B. Hicks *et al.* (World Scientific, Singapore, 1994), Vol. 4, p. 500.
[4] Y. Fukuda *et al.*, Phys. Lett. B **335**, 237 (1994).
[5] J.G. Learned, S. Pakvasa, and T.J. Weiler, Phys. Lett. B **207**, 79 (1988).
[6] V. Berger and K. Whisnant, Phys. Lett. B **209**, 365 (1988).
[7] K. Hidaka, M. Honda, and S. Midorikawa, Phys. Rev. Lett. **61**, 1537 (1988).
[8] S. Midorikawa, M. Honda, and K. Kasahara, Phys. Rev. D **44**, 3379 (1991).
[9] R.M. Bionta *et al.*, Phys. Rev. D **38**, 768 (1988).
[10] Y. Oyama *et al.*, Phys. Rev. D **39**, 1481 (1989).
[11] W. Frati, T.K. Gaisser, A.K. Mann, and T. Stanev, Phys. Rev. D **48**, 1140 (1993).
[12] L.V. Volkova, Yad. Fiz. **31**, 1510 (1980) [Sov. J. Nucl. Phys. **37**, 784 (1980)].
[13] K. Mitsui, Y. Minorikawa, and H. Komori, Nuovo Cimento C **9**, 995 (1986).
[14] A.V. Butkevich, L.G. Dedenko, and I.M. Zhelsnykh, Yad. Fiz. **50**, 142 (1989) [Sov. J. Nucl. Phys. **50**, 90 (1989)].
[15] P. Lipari, Astropart. Phys. **1**, 195 (1993).
[16] T.K. Gaisser, T. Stanev, and G. Barr, Phys. Rev. D **38**, 85 (1988).
[17] G. Barr, T.K. Gaisser, and T. Stanev, Phys. Rev. D **39**, 3532 (1989).
[18] E.V. Bugaev and V.A. Naumov, Phys. Lett. B **232**, 391 (1989).
[19] H. Lee and Y. Koh, Nuovo Cimento B **105**, 884 (1990).
[20] M. Honda, K. Kasahara, K. Hidaka, and S. Midorikawa, Phys. Lett. B **248**, 193 (1990).
[21] D.H. Perkins, Astropart. Phys. **2**, 249 (1994).
[22] W.R. Webber and J.A. Lezniak, Astrophys. Space Sci. **30**, 361 (1974).
[23] J.F. Ormes and W.R. Webber, in *Proceedings of the Ninth International Cosmic Ray Conference*, London, 1965, edited by A. C. Stickland (The Institute of Physics and the Physical Society, London, 1965), Vol. 1, p. 349.
[24] W.R. Webber, J.A. Lezniak, J.C. Kish, and S.V. Damle, Nature Phys. Sci. **246**, 96 (1973).
[25] M. Ryan, J.F. Ormes, and V.K. Balasubrahmanyan, Phys. Rev. Lett. **28**, 985 (1972).
[26] L.H. Smith *et al.*, Astrophys. J. **180**, 987 (1973).
[27] K.C. Ananda *et al.*, Proc. Ind. Acad. Sci. **67**, 138 (1968).
[28] R.P. Verma *et al.*, Nature (London) **240**, 135 (1972).
[29] V.K. Balasubrahmanyan *et al.*, Astrophys. J. **140**, 109 (1973).
[30] E. Julisson, in *Proceedings of the Thirteenth International Cosmic Ray Conference*, Denver, Colorado, 1973, edited by R.L. Chasson (University of Denver, Denver, 1973), Vol. 1, p. 178.
[31] E.S. Seo *et al.*, in *Proceedings of the Twenty Second International Cosmic Ray Conference*, Dublin, Ireland, 1991, edited by M. Cawley *et al.* (Reprint Ltd., Dublin, Ireland, 1991), Vol. 2, p. 627.
[32] K. Nagashima *et al.*, Nuovo Cimento C **12**, 173 (1989).
[33] D.R. Barraclough *et al.* (IAGA Division I Working Group 1), J. Geomagn. Geoelectr. **37**, 1157 (1985).
[34] K. Asakimori *et al.*, in Cosmic Ray Conference [3], Vol. 2, p. 21.
[35] K. Asakimori *et al.*, in *Cosmic Ray Conference* [3], Vol. 2, p. 25.
[36] I.P. Ivanenko *et al.*, in *Cosmic Ray Conference* [3], Vol. 2, p. 17.
[37] J. Dwyer *et al.*, in *Cosmic Ray Conference* [3], Vol. 1, p. 587.
[38] M. Ichimura *et al.*, Phys. Rev. D **48**, 1949 (1993).
[39] M. Simon *et al.*, Astrophys. J. **239**, 712 (1980).
[40] J.J. Engelmann *et al.*, Astron. Astrophys. **96**, 233 (1990).
[41] D. Muller *et al.*, Astrophys. J. **374**, 356 (1991).
[42] J. Buckley *et al.*, in *Proceedings of the Twenty Third International Cosmic Ray Conference* [35], Vol. 1, p. 599.
[43] M. Nagano *et al.*, J. Phys. G **10**, 1295 (1984).
[44] Y. Shirasaki *et al.*, in *Cosmic Ray Conference* [3], Vol. 2, p. 85.
[45] N.L. Grigorov *et al.*, in *Proceedings of the Twelfth International Cosmic Ray Conference*, Hobart 1971, edited by A. G. Fenton (University of Tasmania, Hobart, Tasmania, Australia, 1971), Vol. 5, p. 1746.
[46] K. Hänssget and J. Ranft, Comput. Phys. **39**, 37 (1986).
[47] K. Hänssget and J. Ranft, Nucl. Sci. Eng. **88**, 537 (1984); **88**, 551 (1984); Comput. Phys. **39**, 37 (1986).
[48] B. Nilsson-Almqvist and E. Stenlund, Comput. Commun. **43**, 387 (1987).
[49] T. Sjöstrand and M. Bengtsson, Comput. Commun. **43**, 367 (1987).
[50] See the World-Wide Web address; http://cpsun1.b6.kanagawa-u.ac.jp. See also K. Kasahara, S. Torii, and T. Yuda, in *Proceedings of the Sixteenth International Cosmic Ray Conference*, Kyoto, Japan, 1979 (Institute For Cosmic Ray Research, Tokyo, Japan, 1979), Vol. 13, p. 70.
[51] T. Eichten *et al.*, Nucl. Phys. **B44**, 333 (1972).
[52] J. Papp *et al.*, Phys. Rev. Lett. **34**, 601 (1975); **34**, 991 (1975).
[53] G.J. Alner *et al.*, Z. Phys. C **33**, 1 (1986).
[54] K. Alpgard *et al.*, Phys. Lett. **112B**, 88 (1982).
[55] Particle Data Group, L. Montanet *et al.*, Phys. Rev. D **50**, 1173 (1994), pp. 1196 and 1202.
[56] S. Hayakawa, Phys. Rev. **108**, 1533 (1957).
[57] N. Brene, L. Egrard, and B. Qvist, Nucl. Phys. **22**, 553 (1961).
[58] T. Akesson *et al.*, Phys. Rev. Lett. **55**, 2535 (1985).
[59] L.V. Volkova (private communication).
[60] S.E. Forsythe, *Smithsonian Physical Tables* (Smithsonian Institution Press, Washington, DC, 1969).
[61] M. Takita, Ph.D. thesis, University of Tokyo, 1989, Report No. ICR-Report-186-89-3 (unpublished).
[62] O.C. Allkofer, K. Carstensen, and W.D. Dau, in *Proceedings of the Twelfth International Cosmic Ray Conference* [45], Vol. 4, p. 1314; Phys. Lett. **36**, 424 (1971).
[63] B.C. Rastin, J. Phys. G **10**, 1609 (1984).
[64] C.A. Ayre *et al.*, J. Phys. G **1**, 584 (1975).
[65] C.A. Ayre *et al.*, in *Proceedings of the Thirteenth International Cosmic Ray Conference* [30], Vol. 3, p. 1754.
[66] B.C. Nandi and M.S. Sinha, J. Phys. G **5**, 1384 (1972).
[67] B.J. Bateman *et al.*, Phys. Lett. **36B**, 144 (1971).

[68] P.J. Hayman and A.W. Wolfendale, Proc. Phys. Soc. London **80**, 710 (1962).
[69] T.H. Burnett *et al.*, in *Proceedings of the Thirteenth International Cosmic Ray Conference* [30], Vol. 3, p. 1764.
[70] O.C. Allkofer *et al.*, in *Proceedings of the Seventeenth International Cosmic Ray Conference*, Paris, 1981, edited by Ch. Ryter (Centre d'Etudes Nucléaires de Saclay, Gif-sur-Yvette, France, 1981), Vol. 10, p. 254; O.C. Allkofer *et al.*, Nucl. Phys. **B259**, 1 (1985).
[71] S. Matsuno *et al.*, Phys. Rev. D **29**, 1 (1984).
[72] B.C. Rastin, J. Phys. G **10**, 1629 (1984).
[73] I.C. Appleton, M.T. Hougue, and B.C. Rastin, Nucl. Phys. **B26**, 365 (1971).
[74] B.C. Nandi and M.S. Sinha, Nucl. Phys. **B40**, 289 (1972).
[75] J.M. Baxendale, C.J. Hume, and M.G. Thompson, J. Phys. G **7**, 781 (1975).
[76] M. Circella *et al.*, in *Cosmic Ray Conference* [3], Vol. 4, p. 503.